EFFECT OF INHERENT MICROTEXTURE ON STRAIN HETEROGENEITY IN ROLLED MAGNESIUM AZ31

by

İbrahim Buğra Üçel

B.S., Mechanical Engineering, Boğaziçi University, 2015

Submitted to the Institute for Graduate Studies in
Science and Engineering in partial fulfillment of
the requirements for the degree of
Master of Science

Graduate Program in Mechanical Engineering
Boğaziçi University

2018

ACKNOWLEDGEMENTS

First, I would like to thank my family for thier support and contribution. My mother, Müjgan Üçel, my father, Hasan Üçel, and of course my beloved sister, Rüya Üçel, their existances have always been a motivation to me.

It was an honor to work with Assoc. Prof. C. Can Aydıner. His contributions throught my undergraduate and graduate years have been invaluable.

I would also like to thank Assoc. Prof. Çetin Yılmaz and Assoc. Prof. Erdem Alaca. Their constructive feedbacks has enhanced the content of this study.

I appreciate companies and supports of my lab mates, Enver Kapan, Nima Shafaghi, Sevinç Uçar, Olcay Türkoğlu, Mona Raessi, Necdet Ali Özdür and Güneş Ece Akalın. They have been the best colleagues that I could ever have.

This work supported by the Scientific and Technological Research Council of Turkey (TÜBİTAK), Grant No: 114M215.

ABSTRACT

EFFECT OF INHERENT MICROTEXTURE ON STRAIN HETEROGENEITY IN ROLLED MAGNESIUM AZ31

The level of utilization of magnesium alloys in engineering practice is steadily increasing, mainly due to their high specific strength. Their complex mechanical behavior, however, requires characterization at microstructural length scales to achieve reliable designs. In this study, mesoscale strain fields are investigated in detail on wrought Magnesium AZ31. For this purpose, two dogbone samples cut from orthogonal faces of a rolled Magnesium AZ31 plate are subjected to uniaxial tension along the rolling direction. In these experiments, using in-situ multiscale digital image correlation technique (DIC), the deformation heterogeneities in elastic and early plastic regime are investigated. DIC combination maps in terms of strain and rotation that depict the deformation character are produced. Strain heterogeneity patterns are observed as flat bands and non-45° bands on the surface normal to transverse direction (TD) of the plate while flat bands and thick horizontal localization structures are noted on the orthogonal normal-direction (ND) surface. Strain localization structures are distinguished by applying data filters. Then, the spatial characteristics of individual localization structures are explained with the content of rotation and Poisson's ratio. Detailed measurement over two orthogonal faces allows volumetric interpretation of plastic localization structures. Thus, it is understood that the non-45° bands observed on TD-normal surface are widespread three dimensional structures which appear almost horizontal on the ND-normal surface. It is shown that these bands play dominant role in material deformation despite their low volume fractions. Their association with heterogeneous microstructure that is inherited from the rolling process is investigated with electron back scattering diffraction.

ÖZET

KALITSAL MİKROTEKSTÜRÜN HADDELİ MAGNEZYUMDA GERİNME DÜZENSİZLİKLERİNE ETKİSİ

Magnezyum alaşımlarının mühendislikteki kullanım düzeyleri, temelde yük-sek özgül dayanımları sebebiyle, gittikçe artmaktadır. Öte yandan karmaşık mekanik davranış, sağlıklı tasarımlar için alt ölçek belirlemelerini gerekli kılmaktadır. Bu çalışmada, biçimlendirilmiş Magnezyum alaşımı AZ31 üzerinde, mikroyapısal orta ölçekte gerinme alanları detaylıca incelenmiştir. Bu amaç için, haddeli Magnezyum AZ31 levhanın dik yüzeylerinden kesilen iki çekme numunesine hadde yönünde çekme testi uygulanmıştır. Bu testlerde, çoklu ölçekte yerinde (in-situ) dijital imge korelasyonu (DIC) yöntemiyle elastik ve erken plastik bölgelerde deformasyon düzensizlikleri belirlenmiştir. Saha değişkenleri cinsinden deformasyon karakterini gösteren mikroskobik DIC birleşim haritaları sunulmuştur. Plaka enine dik yüzeyde gerinme yığılmaları iki farklı desende (yassı ve yüksek açılı şeritler) oluşmuştur. Plaka normaline dik yüzeyde ise yassı ve kalın yatay yığılma desenleri kaydedilmiştir. Her iki numune üzerinde veri süzgeçleri yardımıyla belirli bir yığılma yapısına özgü gerinmeler filtrelenmiştir. Tekil yığılma yapılarına özgü bu deformasyon alanlarının uzamsal özellikleri rotasyon ve Poisson oranlarıyla açıklanmıştır. Plastik bölge boyunca birbirine dik iki malzeme yüzeyinde meydana gelen karakteristik gerinme yığılmaları hacimsel olarak bütünleştirilmiştir. Bu sayede enine dik yüzeydeki yüksek açılı şeritlerin, diğer yüzeyde yaklaşık yatay gözüken yaygın üç boyutlu yapılar olduğu anlaşılmıştır. Görece düşük hacim oranına rağmen, malzeme deformasyonunda hakim olan bu şeritlerin mikroyapı ve kalıtsal miktotekstürle ilişkisi elektron mikroskobi elektron geri saçılım kırınımı sonuçlarıyla incelenmiştir.

TABLE OF CONTENTS

LIST OF FIGURES

LIST OF TABLES

LIST OF SYMBOLS

α	Initial micro-DIC load point
$\delta\varepsilon_{yy}$	Standard deviation of axial strain
$\delta\varepsilon_{xx}$	Standard deviation of transverse strain
ε_{yy}	Axial strain
ε_{yy}^{lim}	Limiting value for axial strain
ε_{xx}	Transverse strain
Θ	Rotation angle
ν	Effective Poisson's ratio
ν^{ind}	Individual Poisson's ratio
σ	Stress
ω_{xy}	Rotation
ω_{xy}^{lim}	Limiting value for rotation

LIST OF ACRONYMS/ABBREVIATIONS

2D	Two dimensional
3D	Three dimensional
BCC	Body-centered-cubic
CTW	Compressive Twin
DIC	Digital Image Correlation
DRX	Dynamic Recrystallization
DTW	Double Twin
EBSD	Electron back scattering diffraction
EDM	Electrical Discharge Machining
FCC	Face-centered-cubic
HCP	Hexagonal-close-packed
ND	Normal Direction
NDO	Normal Direction Observation
RD	Rolling Direction
SF	Schmid Factor
TD	Transverse Direction
TDO	Transverse Direction Observation
TTW	Tensile Twin

1. INTRODUCTION

1.1. Motivation

Strength and formability are two crucial parameters for a material used in engineering applications. In this regard, metallic materials have wide range of use. With the obvious need to improve energy efficiency in many key sectors like transportation, strength to weight ratio (specific strength) appears as a critical material property [1]. As the lowest density metal (1.74 g/cm^3) with considerable strength reaching 300 MPa with proper alloying and processing, Magnesium is a significant and promising material in this respect. However; formation of sharp textures in formed Mg and Mg alloys through typical processes like rolling and extrusion causes high complexity in deformation behavior in the form of pronounced anisotropy in constitutive behavior and severe load path dependence. Load path dependence is usually observed in uniaxial experiments with very heavy tension-compression anisotropy in the character and form of stress-strain curves.

To come up with reliable mechanical designs with this material, a more fundamental description of the material has to be made, one that accounts for operation of deformation micromechanisms. Deformation twinning mechanisms are an important factor underlying the complexity in these materials, which are activated in addition to dislocation slip, the predominant mechanism of metal deformation [2]. Scientifically, Magnesium alloys are also considered as the model materials for twinning physics particularly due to the profuse activity of the tensile twin on selected load paths. Consequently, there is a bias toward studying the wrought Magnesium alloy behavior in such twinning configurations when tensile twin dominates near all strain accommodation. However, in the opposite load paths, when twinning is not profusely activated, Magnesium deformation is still extremely compound, requiring the collaboration of multiple slip/twin systems. Further, understanding the deformation along this path is at least as important from an engineering (failure prediction) perspective, since the majority

of real-life loads have a cyclic nature.

This study attempts to provide novel multi-scale experimental evidence that clearly lays out the operation of the collaborative deformation structures when the material is loaded in this load path. The physics revealed can be combined with the existing investigations on profuse-twinning behavior [3] to better understand the cyclic deformation behavior of the material. The multi-scale experimental results have the potential of leading the way for the necessary multi-scale predictive modeling.

1.2. Background

Dislocation slip is the typical mechanism that facilitates plastic deformation in ductile metals. Ductile metals can undergo an arbitrary shape change which requires at least five independent slip systems. This requirement is easily met in typical body-centered cubic (BCC) and face-centered cubic (FCC) materials. However, in hexagonal-close-packed (HCP) materials such as Mg, Ti and Zr the number of easy slip systems can be below 5. Among characteristic slip systems of HCP materials, $< a >$ basal slip $< a >$ prismatic slip as shown in Figure 1.1 (b) have only 2 independent slip systems each. Apart from $< c + a >$ type II pyramidal slip, which is known to be extremely hard in Magnesium alloys, none of the slip systems shown can provide normal strain along the c-axis. However clearly, strain accommodation along the c-axis is required to undergo arbitrary shape change. The heavy employment of deformation twinning (Figure 1.1 (d)) by these materials can be understood in this context, since it is another mechanism that can yield straining along the c-axis.

Twinning entails diffusionless transformation of a region (typically a band) where the crystalline lattice becomes the mirror image of the original lattice about a particular crystallographic plane. Figure 1.2 shows this for the most typical $\{10\bar{1}2\}$-twin for HCP lattices. Unlike dislocation slip, deformation twinning can activate only in one shear sense. That is why twin mechanisms are called 'unidirectional' or 'unipolar'. To exemplify, if tensile loading activates twinning in a crystallite; compression will not.

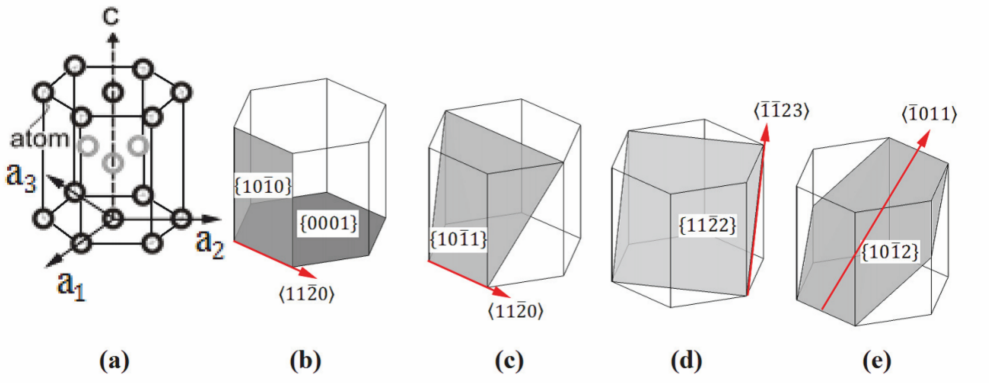

Figure 1.1. (a) Unit cell for an hcp crystal, (b) basal and prismatic slip systems, (c) type I pyramidal slip system, (d) type II pyramidal slip system, (e) tensile twin system.

As demonstrated in Figure 1.2, twinning transformation brings about a very sizeable shear strain. This transformation typically occurs suddenly and generates substantial strain localization in and about the twin region. So inside a polycrystalline aggregate, strain localization caused by twinning in a particular crystallite can introduce high levels of intragranular and intergranular strain heterogeneity.

Strain heterogeneity levels are further strongly related to texture and the differentials between the activation stresses of accessible slip systems. For instance, in α-Titanium $< a >$ prismatic slip is the easiest slip system. The following easy glide systems $< a >$ basal and $< c + a >$ pyramidal slip require a similar shear stress to be activated [4]. This near uniformity of activation ease of different slip systems allow alternative paths for strain accommodation and resist the development of very sharp textures during the forming processes. Specifically in α-Titanium, the impurity content affects deformation aspects of the material as well. Low symmetry of hexagonal unit cell due to interstitial oxygen and hydrogen atoms impedes profuse twinning as well as the strain heterogeneity that would stem from twinning [5].

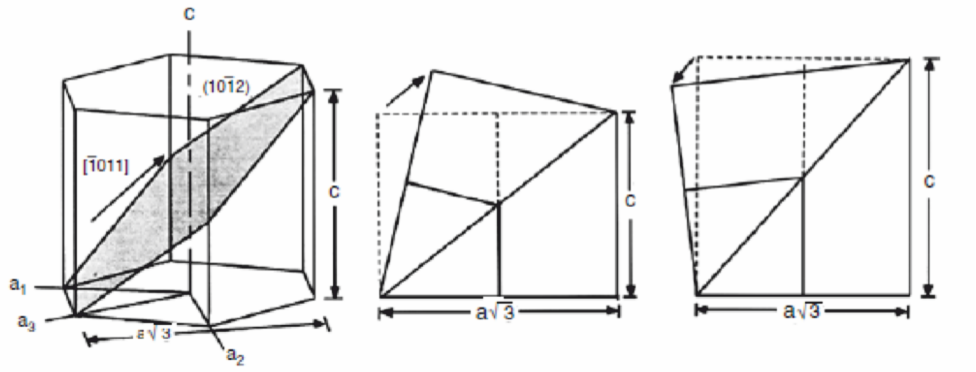

Figure 1.2. Twinning in HCP materials with c/a< $\sqrt{3}$ (middle) and c/a> $\sqrt{3}$ (right), reproduced from [6]

However; unlike α-Titanium $\{10\bar{1}2\} < \bar{1}011 >$ tensile twinning (TTW) is a prominent deformation system in polycrystalline Mg alloys. $< a >$ basal slip is by far the easiest slip system in Mg and the next easy glide system ($< a >$ prismatic slip) requires vastly greater activation stress [7]. This makes $\{10\bar{1}2\}$ TTW is the second easiest deformation mechanism. With these deformation modes, sharp crystallographic textures develop in forming processes like rolling and extrusion. The rolling texture entails preferential alignment of c-axes whereas extrusion texture is characterized by a polar symmetrical distribution of c-axes confined in the same plane [8]. These clear-cut textures, in turn, promote the plastic anisotropy of the resulting polycrystalline aggregate. Loaded along their respective drawing directions, both rolled [7,9,10] and extruded [11] materials show intense tension-compression anisotropy, since, only in one sense of the load, the $\{10\bar{1}2\}$ TTW dominates the strain accommodation.

Complexity and anisotropy of deformation mechanisms naturally promote strain heterogeneity. A key concept for constitutive behavior and particularly failure, strain heterogeneity levels can be determined by methods like digital image correlation (DIC) that offer high spatial resolution [12]. Indeed, DIC strain mapping has been used to elucidate wrought Magnesium deformation at multiple length scales from macroscopic [13, 14] to microscopic [optical [3], SEM [15]]. In principal, twinning modes are susceptible to make a severe impact on strain heterogeneity levels. They are large,

abruptly emerging defects that bring about a fixed transformation strain. Further, twin transmission [16, 17], namely, a twin to prompt twinning in the next crystallite, is an important factor that can precipitate strain heterogeneity at a higher length-scale. Consequently, it is of great interest to investigate strain heterogeneity when the $\{10\bar{1}2\}$ twin mode is profusely activated in these materials. Macroscopically, deformation in this regime presents little hardening, typified with a twin plateau on the stress-strain curves. Strain heterogeneity levels, on the other hand, show pivotal dependence on texture as outlined in rolled versus extruded material comparison of Kapan et al. (2017) [14]. Over the $\{10\bar{1}2\}$ TTW plateau, rolled material is established to be a worst case in terms of strain heterogeneity, revealing sharp and macroscopic shear band structures at the macroscale. Aydiner et al. (2014) [3], the method precursor of the current study, zoomed further into these bands. There, DIC is conducted at the optical microscopy resolution but its coverage is extended to the macroscopic length scale by area scanning. The resulting combination strain maps resolved the make-up of the macroscopic shear bands as another set of mesoscopic deformation bands with very high strain heterogeneity. Bands at both length scales appear $\pm 45^\circ$ to the load, agreeing with maximum shear angle for the uniaxial macroscopic stress. While $\pm 45^\circ$ strain localization maybe considered typical in cooperative intergranular deformation [12, 18, 19] , there is an outstanding structure in this case: Out of the infinitely many maximum shear planes about the load axis, bands virtually form only over a specific doublet that bisect the normal direction (ND) of the plate and the perpendicular compression axis. The root cause is that the activated $\{10\bar{1}2\}$ twin planes on the preferred orientations (c-axes // ND) are distributed in proximity of these two specific planes and the strictly two-dimensional $\pm 45^\circ$ patterns are a manifestation of abruptly progressing $\{10\bar{1}2\}$ TTW networks.

Under reversed loading, that is compression along c-axis or tension normal to c-axis, the absence of $\{10\bar{1}2\}$ tensile twinning forces the material to activate other deformation mechanisms for strain accommodation along c-axis. In this regard, early studies that focus on single crystal Mg under c-axis compression [20, 21] and tension normal to c-axis [22] state the activation of $\{10\bar{1}1\}$ and $\{10\bar{1}3\}$ compressive twins. How-

ever; these twin systems produce small twin bands unlike $\{10\bar{1}2\}$ tensile twinning and are largely unstable: Typically rotated bands of $\{10\bar{1}1\}/\{10\bar{1}3\}$ twin become prone to further $\{10\bar{1}2\}$ tensile twinning in their volume as shown in Figure 1.3. More precisely, the region that is imposed to $\{10\bar{1}1\}/\{10\bar{1}3\}$ compressive twin immediately retwins with $\{10\bar{1}2\}$ system. This phenomenon is called double twinning or retwinning [23,24].

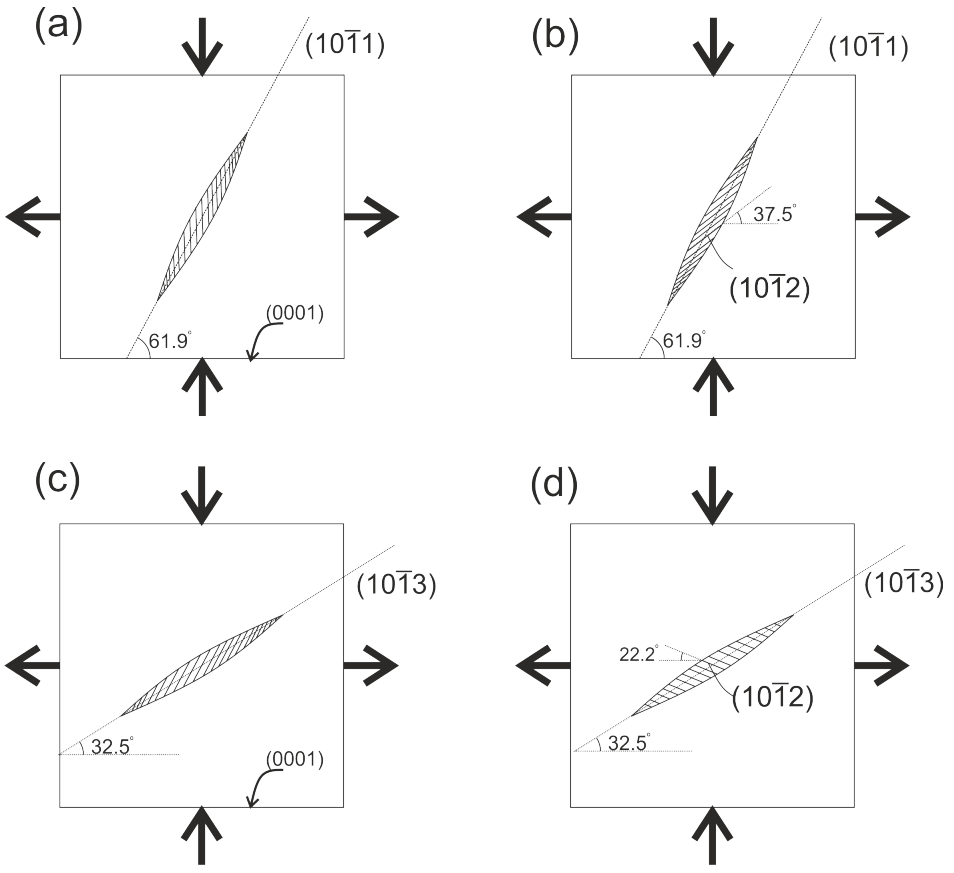

Figure 1.3. Scheme of $\{10\bar{1}1\}$ (a) and $\{10\bar{1}3\}$ (c) compressive twins and their respective (b), (d) $\{10\bar{1}2\}$ double twins

For polycrystalline aggregates of Mg alloys under c-axes compression, mechanisms for strain accommodation are compound. Among the classical references of polycrystalline Mg that considers this type load path, Couling et. al. 1959 [25] concentrates on the formability of hot rolled Mg-RE (rare earth element) alloys under cold rolling. Cold rolling specifically implies c-axis compression on the abundant orientations with an out-of-plane constraint. On TD (transverse direction) surface of the

cold-rolled material, they observe a network of shear band structures that stray from the typical $\pm 45^\circ$ with polarized microscopy. Other studies that consider load configurations that are within the general umbrella of imposing c-axis compression on the preferred orienations, e.g., uniaxial experiments of tension in RD and compression in ND, similar shear band patterns are noted [13,26–28]. In a similar manner, some recent cold rolling studies observe the bands with electron-back-scatter diffraction (EBSD), in particular using kernel average misorientation (KAM) maps [29,30]. The (cold) rolling literature naturally considers aspects beyond the scope of this study and relevant for rolling performance, e.g., the effect of temperature [28, 31] strain rate and alloying elements [25, 29, 30].

As for the physical root of this particular band of strain localization, the main reason stated in the literature is the existence of a microstructure heterogeneity that persists from previous rolling operations even after annealing [32]. This historical effect states that there are bands/regions of softer-oriented grains that deviate from the overall texture, leading to a strain localization explicable by preferential easy glide [29]. [The formation of this non-uniform microstructure, on the other hand, is also likely due to DTW and dynamic recrystallization during the previous processing [25, 29, 33, 34] These factors are not necessarily mutually exclusive explanations; since there are observations of DTW in the non-45° bands as well as heavy basal slip activity [30]. Non-45° band structures have been specifically related to material failure [26, 28] and, of course, there are many generic references that associate failure with DTWs [35, 36].

1.3. Scope

Studies that consider RD-tensioned or ND-compressed Mg rolled plate samples observe shear bands and, in general, associate these strain heterogeneities with failure. However, the findings of the literature described in the previous Section is by and large qualitative and do not present complete spatial aspects of strain heterogeneities that emerge in Mg aggregates where c-axes of the preferred orientations are compressed.

In this study, strain heterogeneity structures that are associated with c-axis-compression of rolled Magnesium AZ31 is studied with scanning microscopic DIC that is complemented with macroscopic DIC that is applied on orthogonal material surfaces. The technique is in situ with stepwise loading and the focus will be over initial stages of plasticity capturing the emergence and subsequent intensifying of strain localization structures. Multiscale strain measurement will allow directly bridging mesoscale localization structures to macroscale. The results will be quantitative in terms of strain and rotation. The method offers immense statistical significance (over 10^6 grains in the analysis region) with granular resolution. Load will be applied with tension along rolling direction (RD). To assess the three-dimensional nature of mesoscale strain localization structures, two RD-loaded samples is considered such that the microscopic imaging plane is perpendicular to transverse direction (TD) in one and ND in the other. This will effectively amount to being able to apply scanning microscopic DIC on both faces of the same sample under RD-tension.

2. EXPERIMENTAL METHOD

2.1. Material and sample preparation

Mg AZ31 (3% Aluminum, 1% Zinc) with rolling texture is purchased from Alfa Aesar. The overall texture of the material is presented with a pole figure in Figure 2.1-(a). The data of this figure is collected with a Panalytical X-Pert Pro MPD four-circle diffractometer and processed Matlab MTEX package. The pole figure complies with the typical sharp texture of rolled Magnesium, where c-axes of prefered orientation are aligned with the normal direction (ND).

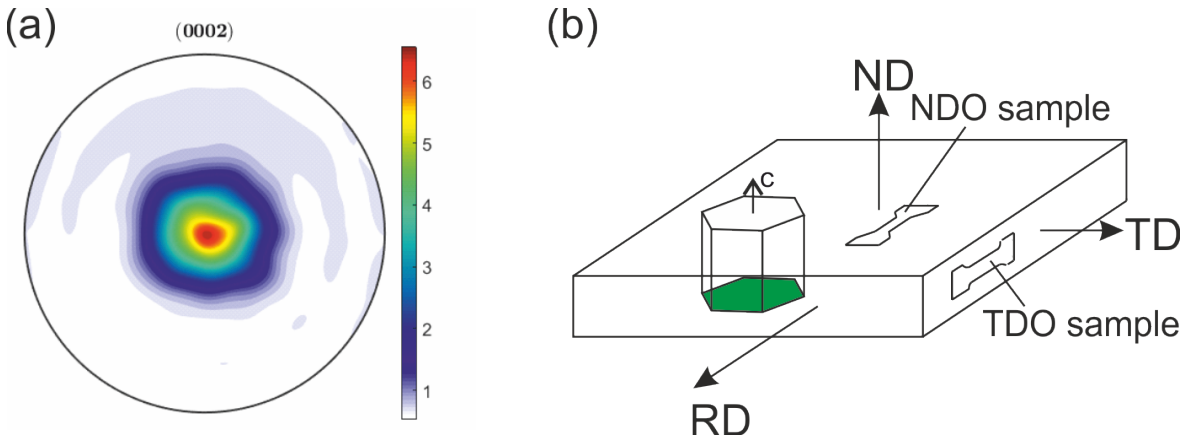

Figure 2.1. Texture of MgAZ31 (a) and the sketch of rolling slab including representative crystal structure indicating the overall texture and configurations of dogbone samples (b)

Two AZ31 dogbone sample specimens with 3x3 mm^2 of gage section area and 8 mm gage section length are prepared for uniaxial tensile testing. Load axis for both is the rolling direction (RD). Two prismatic dogbone specimens are cut out with wire EDM (electro discharge machining) along the RD direction. Their extraction orientation, however, is shifted by 90° with respect to each other about the load axis. Hence, grip (top) plane of the first sample is normal to TD and the second sample is normal to ND as indicated in 2.1(b). Due to the fact that both specimens are tensioned

along RD and their observation planes are normal to TD and ND, hereafter the samples will be respectively called as TDO and NDO, where 'O' indicates their corresponding observation plane (see Figure 2.4(b)).

To make a mesoscopic length-scale DIC observation on sample surfaces, metallographic procedure including grinding, polishing and etching is applied on both specimens. Dogbone specimens are mounted before surface treatment. The reason why specimens are mounted before metallographic treatment is once again to prevent permenant deformation on the surface during grinding process. After mounting, top surfaces of the specimens are grinded progressively using 1200P down to 2500P sandpaper. Next, 50 nm colloidal silica solution is used to polish material surface. After obtaining mirror-like surfaces, materials are etched with picric acid solution (0.56 gr picric acid, 1.5 ml acetic acid, 1.5 ml distilled water and 12 ml ethanol of 99 % purity). As a final step, average grain size is determined as 11 μm using linear intercept method. The resulting picture of etched MgAZ31 sample is shown in Figure 2.2.

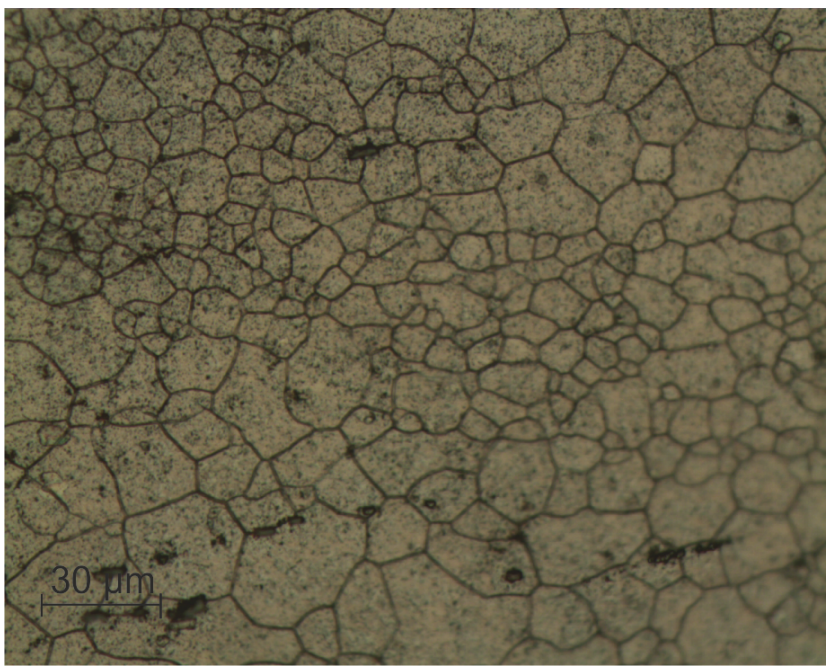

Figure 2.2. Microstructure of a typical TDO sample

The last stage of sample preperation is to create a speckle pattern on top and side surfaces of each specimen for digital image correlation (DIC) (see section 2.3 for detailed explanation) measurement. For microscopic DIC patterning on the top surfaces Iwata air brush is used with a dye solution of 2 drops of black dye and 2 ml distilled water. Dye solution is sprayed over the top surface of the dogbone sample from an 8 cm distance as described in Figure 2.3. This speckle pattern for micro-DIC also provides a proper pattern for macroscopic analysis. To generate a viable DIC pattern for side surfaces as well, typical black and white acrylic spray dyes are utilized.

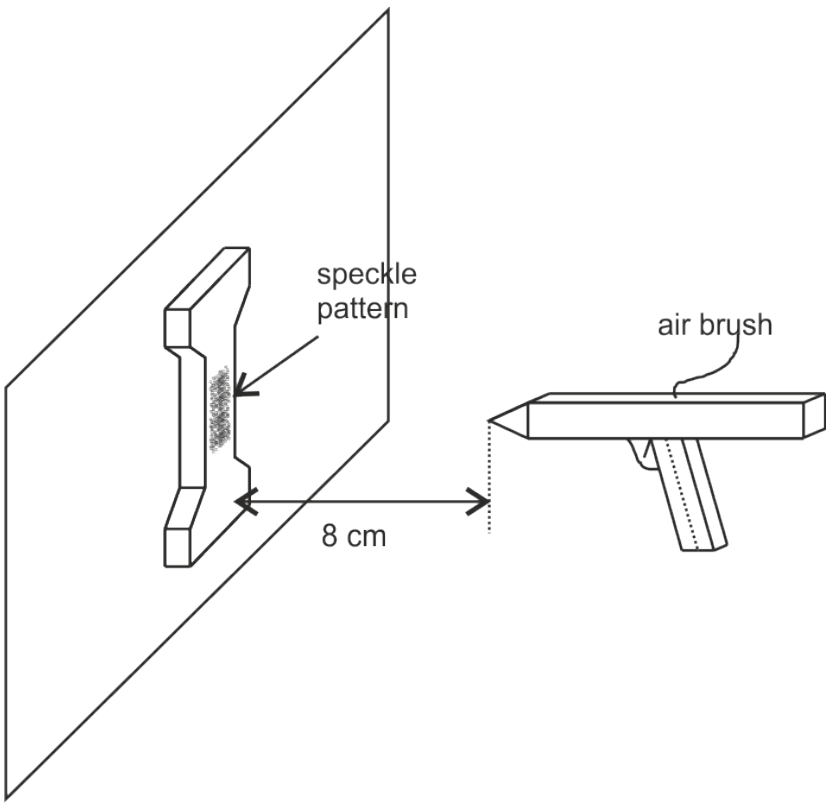

Figure 2.3. Sketch of micro-DIC patterning

2.2. Setup and procedure

The setup comprises positioning, loading and imaging elements sketched in Figure 2.4-(a). X-Y positioning is implemented with Newport ILS-series linear stages which sit under a Newport GTS30V vertical stage that adjusts Z-coordinate. Loading element is a Kammrath&Weiss microscopic load frame with 10 kN capacity. Images are recorded

by two optical lines that utilize AVT Pike F505B cameras with 5 Megapixel CCDs. The macroscopic DIC line is fitted with an Edmund Optics 0.5x telecentric lens with working distance (WD) 110 mm, depth of field (DOF) 2mm, field of view (FOV) 16.7 x 14 mm^2 and optical resolution 6.8 μm/pixel. The microscopic DIC line uses a Navitar Ultrazoom 6000 tube that admits a 10x Mitutoyo infinity-corrected objective at the tip (WD 33 mm, DOF 12 μm, FOV 487 $\times$ 408 m^2, optical resolution 0.199 μm/pixel). All elements of the setup are placed on a vibration-isolated Newport RS4000 optical table.

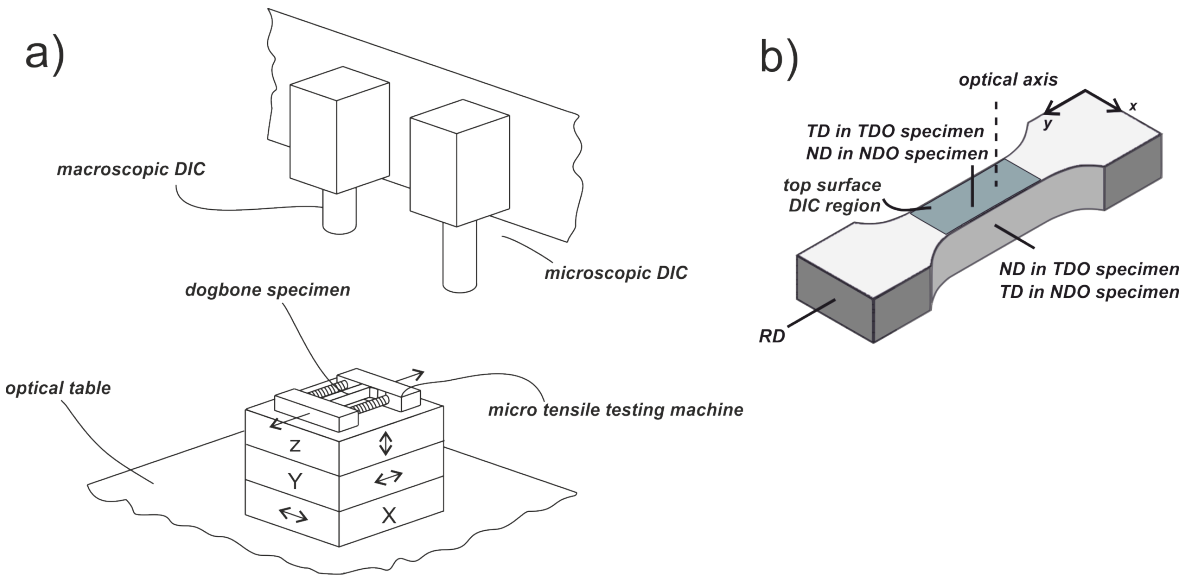

Figure 2.4. Sketch of experimental setup (a) and generic configuration of dogbone specimens (b)

Tensile load is stepwise incremented in position control with average strain steps of 0.05 %. At every load point, the sample is taken under the macroscopic DIC line for direct imaging of the top surface (2.4(b), "macro-top DIC") as well as the side surface (2.4(b), "macro-side DIC") by means of a 45° mirror [14]. At selected load points, the sample top surface is taken under the microscopic DIC line and the surface is area-scanned with a 16x6 microscopic image grid (Figure 2.5(a)). Individual microscopic images (at reference load) are exemplified from the middle of the gage section in Figure 2.5(b). When stitched, the images cover a 5.12 $\times$ 2.43 mm^2 region with approximately 350 Megapixel resolution. This amounts to macro-scale mapping with mesoscale reso-

lution where the monitored approximately 10^6 grains are clearly resolved in the images (Figure 2.5(b)). Figure 2.5(c) demonstrates the stitching operation but only over the selected four frames for clarity. The overlap among frames shown to-scale in Figure 2.4(b) is allowed to obtain continuous strain maps.

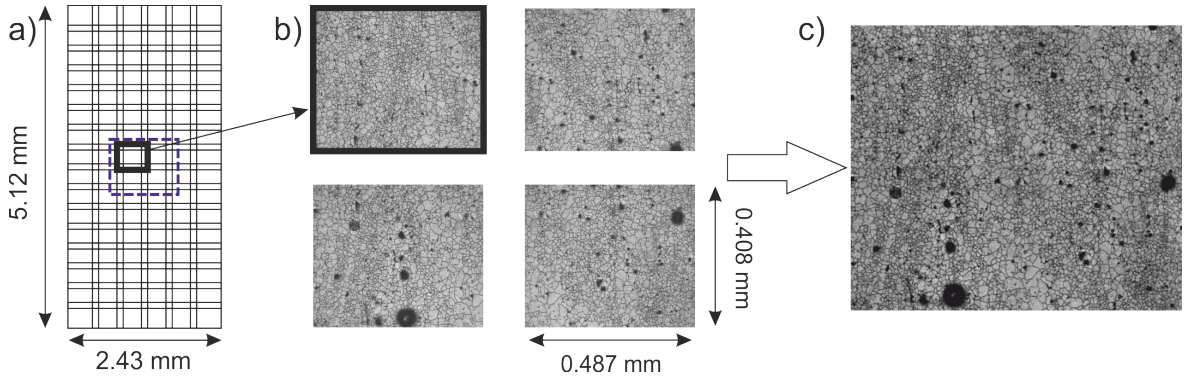

Figure 2.5. Grid and stitch description: part (a) figurative 16x6 overlapping farmes (b) 4 frames on their own in thumbnail size; show frame size on one of them (c) stitched 4 frames

2.3. DIC analysis

Digital Image Correlation (DIC) is a standard technique for strain measurement. Its typical application involves comparison of optical photographs that are recorded from a sample while it undergoes deformation. The points in the reference and deformed images are correlated by tracing of gray scale intensity values of pixels. In this way, displacement field (u, v) is obtained among the two states.

A python^{TM}-based in-house package is coded for DIC analysis and post-processing that also utilizes various open-source packages [37,38]. Here, only major points are provided for brevity; details are given elsewhere [3]: Subset-based DIC analysis is used with first-order formulation whose parameters are x-y displacements u-v and their spatial derivatives [39]. Subsets over uniform grids with 10 pixel spacing is considered for both macroscopic and microscopic analyses. For microscopic DIC, a massive data analysis problem ensues with over 3 million data points per load, tackled with parallelization.

Strains and in-plane rotation on the imaging plane are given in Equation 2.1

$$\varepsilon_{xx} = \frac{\partial u}{\partial x} \qquad \varepsilon_{yy} = \frac{\partial v}{\partial y} \qquad \omega_{xy} = (\frac{\partial u}{\partial y} - \frac{\partial v}{\partial x}) \tag{2.1}$$

The spatial derivatives in Equation 2.1 are recomputed by applying the central-difference formula over the displacement results. The validity of the small strain/rotation formulation is ensured by confirming their virtual equivalence to Lagrangian strain tensor components and rotation via spectral decomposition [40]. Utilized subset sizes are 61x61 pixels ($\sim$ 12 μm $\times$ 12 μm) for microscopic DIC and 81 $\times$ 81 pixels (0.55 mm $\times$ 0.55 mm) for macroscopic DIC. With these parameters, nominal DIC uncertainty, determined by rigid body motion tests are kept within the order of 0.1 %. DIC outlier data points typically take the form of positive-negative value doublets in strain/rotation maps [19]. The microscopic DIC measurements here supersede [3] with the cleanliness of the data maps with the relative lack of outlier doublets (Section 3.2). Another significant improvement is the actual stitching of the strain/rotation data from the 16x6 frame-by-frame analyses to yield spatially continuous microscopic DIC maps. When deformation introduces surface patterns that alter the intensity signature of a subset severely, DIC tracking is physically invalidated. This affect, naturally, is more dominant in the lower-length scale measurement and limits the strain range that can be targeted for useful microscopic DIC data (up to 1 % in [3]). Here, average strain is limited to a nominal 1.5 % in the experiments before DIC losses become prevalent (particularly in the NDO sample, Section 3.2).

2.4. Identification of shear bands

Deformation twinning and dislocation slip fundamentally produce simple shear. When collaborative activity of these processes produce higher length-scale strain localization structures, these also tend to form in shear bands. In this section, ideal simple shear bands with ideal orientations (Figure 2.6) are considered to form a basis

to interpret the actual data in terms of strain components, local Poisson's ratio (ν) and rotation. Under uniaxial load and given sufficient material symmetry, shear bands tend to form $\pm\ \theta$ to the load axis with $\theta\sim$45 typical. Since non-45° bands are also in the context of this study, Figure 2.6a keeps θ generic where $+\theta$ and $-\theta$ simple shear processes are depicted whose plane of shear is the x-y plane. The continuum point rotation (ω_{xy}) is specifically depicted for each. The fact that rotation senses are opposite for the $+\theta$, $-\theta$ families (while they produce equivalent ε_{xx}, ε_{yy}) is taken advantage with a purposeful colorbar that marks positive values with shades of red and negative values with shades of blue [3]. Thus, as visualized on Figure 2.6(c) in 3D, the $-\theta$ band will appear red ($+\omega$) while the $-\theta$ will appear blue ($-\omega$) in terms of rotation. However, if the plane of shear is perpendicular to the observation plane x-y, ω_{xy} will not pick up any signal (Figure2.6(d); band trace shown gray) while strain measure will be intact. In sum, rotation maps are used to identify simple shear processes that are (i) at the length-scale of the measurement and (ii) with plane of shear (approximately) matching the observation plane. Conversely, if the ω_{xy} signal at locality is weak, there are two (not necessarily mutually exclusive) explanations: (i) simple shear processes might be at a lower length scale and their rotation average evened out at the measurement length scale and (ii) plane of shear of the bands is near orthogonal to the observation surface. Further caveats and a more detailed discussion on rotation mapping is provided in [3].

For shearing in the x-y plane, when θ deviates from 45° measurement axes normal strains,and ε_{xx}, are no longer principal (marked with squares on the Mohr's circle of Figure 2.6b). Still, ε_{xx}=-ε_{yy} is maintained with Poisson's ratio ν=1 on the band. This corresponds to ν=0 (no contraction) on the side surface for this isochoric process [14]. Conversely, if the plane of shear is perpendicular to the observation plane for the ideal simple shear structure, ε_{xx}=ν=0 applies on the horizontal strain localization observed in ε_{yy} (Figure 2.6d).

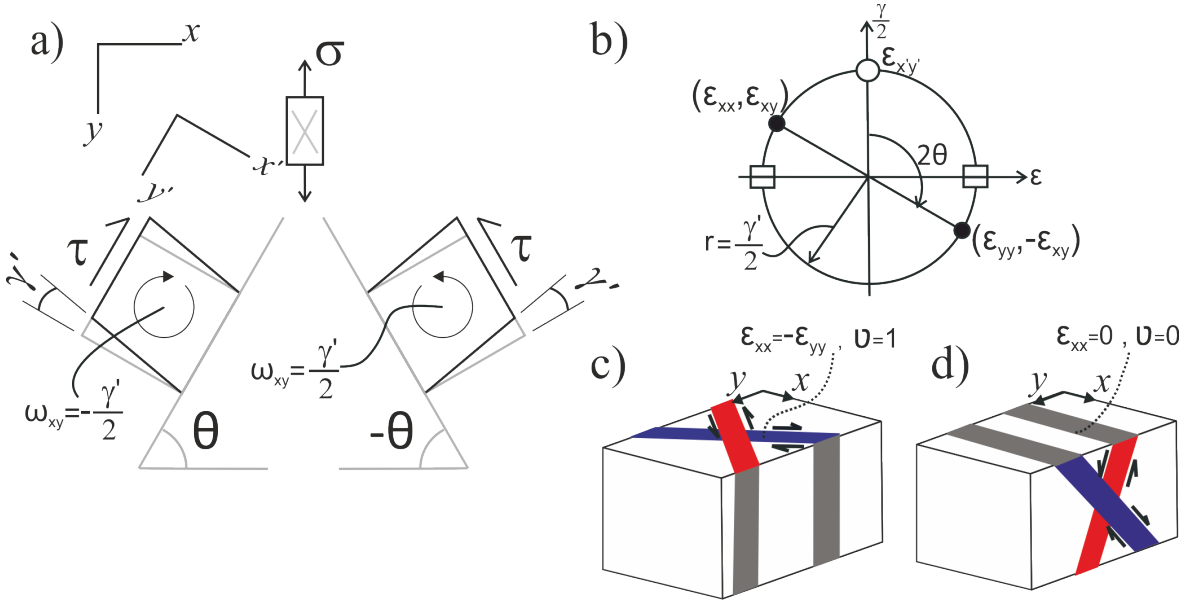

Figure 2.6. In-plane Poisson's ratio of TDO and NDO samples.

3. RESULTS AND DISCUSSION

3.1. Macroscopic results

Stress-strain curves of TDO (solid line) and NDO (dashed line) samples are shown in Figure 3.1. They are constructed based on engineering stress and average strain obtained from macro-DIC analysis. Stress-strain data for macroscopic results are recorded at 36 load points. Among these macro-DIC points, at 5 load points indicated as α, a, b, c and d for TDO sample, and $\alpha*$, a *, b*, c* and d* for NDO sample, DIC gage section area is scanned microscopically (micro-DIC) for mesoscale DIC observations. The limited average strain disparities between micro-DIC load points of TDO and NDO specimens basically stem from unsynchronized experimentation. More specifically, since in both experiments average strain is measured at each load step with no simultaneous-DIC analysis, at some load points discrepancies in overall strain value inevitably arise.

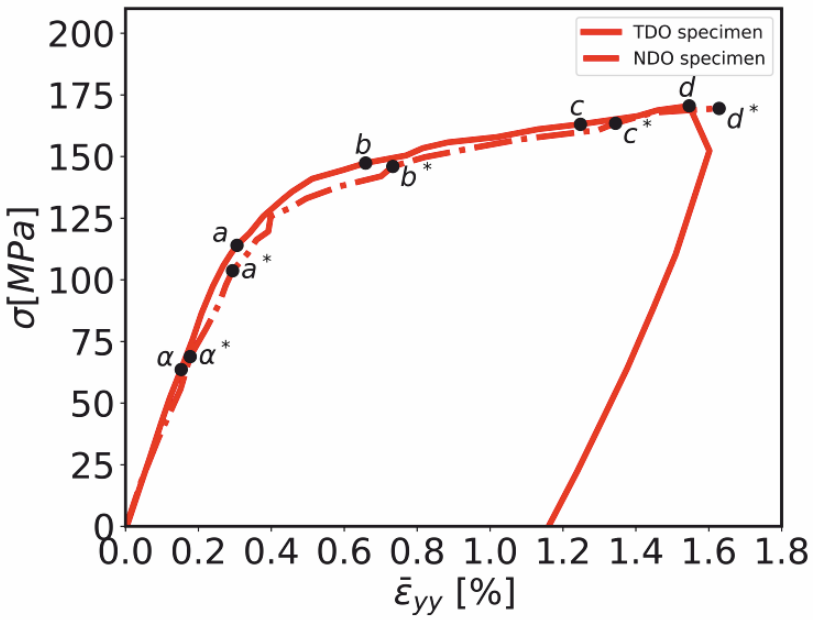

Figure 3.1. Stress-Strain curves of TDO and NDO samples.

RD-tensioned MgAZ31 shows a typical hardening behavior on the stress-strain curve. In fact, load path dependence is notable even at this observation scale. In contrast to appearance of twin plateau after elastic region under RD-compressed Mg [3, 14], the material characteristically hardens under tension normal to c-axes of preferred orientation.

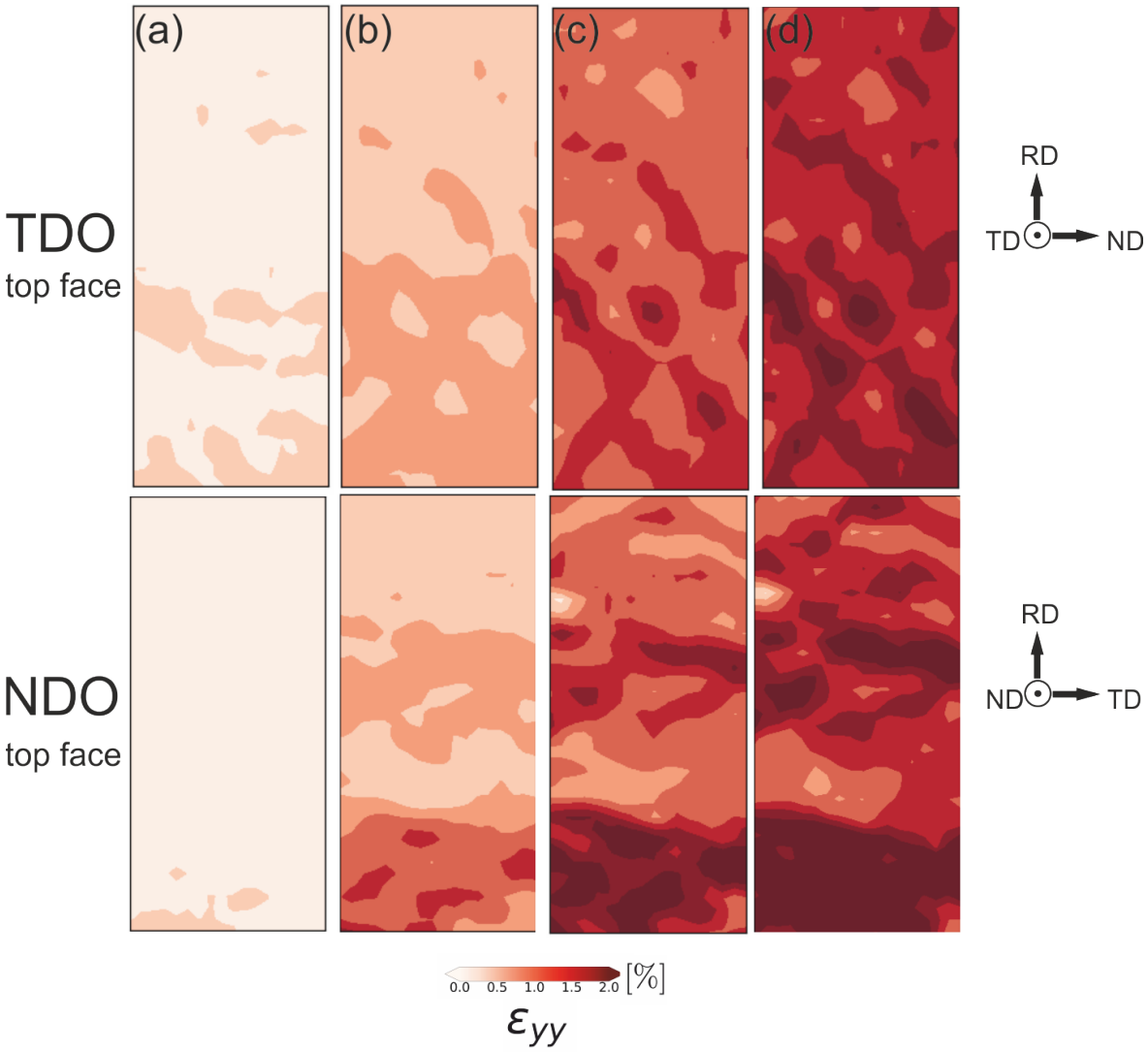

Figure 3.2. Macroscopic ε_{yy} fields of TDO (first row) and NDO (second row) samples at load point a-d

Macroscopic data of micro-DIC load points is presented in Figure 3.2, 3.3 and Table 3.1. Table 3.1 ,here, is prepared to demonstrate average axial and transverse strains and their respective standard deviation values of top faces of TDO and NDO

Table 3.1. Macro-DIC average axial, transverse strain and the respective strandard deviation values of TDO-top and NDO-top field with standard deviation to average ratio

(%)	TDO-Top					NDO-Top				
	$\bar{\varepsilon}_{yy}$	$\|\delta\varepsilon_{yy}\|$	$\bar{\varepsilon}_{xx}$	$\|\delta\varepsilon_{xx}\|$	$\|\delta\varepsilon_{yy}\|$ / $\bar{\varepsilon}_{yy}$	$\bar{\varepsilon}_{yy}$	$\|\delta\varepsilon_{yy}\|$	$\bar{\varepsilon}_{xx}$	$\|\delta\varepsilon_{xx}\|$	$\|\delta\varepsilon_{yy}\|$ / $\bar{\varepsilon}_{yy}$
α	0.15	0.017	-0.04	0.019	0.116	0.17	0.016	-0.05	0.016	0.102
a	0.31	0.029	-0.09	0.021	0.096	0.27	0.0319	-0.09	0.017	0.119
b	0.66	0.117	-0.32	0.091	0.177	0.75	0.276	-0.23	0.108	0.368
c	1.26	0.182	-0.63	0.156	0.145	1.35	0.422	-0.50	0.213	0.312
d	1.62	0.221	-0.79	0.198	0.137	1.69	0.471	-0.67	0.250	0.279

sample. Additionally, $\|\delta\varepsilon_{yy}\|$ / $\bar{\varepsilon}_{yy}$ values for each sample are employed as a parameter to describe the overall strain heterogeneity of the field [14]. Figure 3.2 shows macroscopic contour maps of ε_{yy} at load points a-d of TDO (top) and a^*-d^* of NDO sample (bottom). For simplicity, "$*$" superscript for NDO points will be dropped from this point on and Figure 3.2 labels that correspond to each load stage are marked (a)-(d). ε_{yy} field of point α is excluded in this representation of deformation pictures since it has no noticable heterogeneous strain pattern at this length scale. Histograms of ε_{yy} of top and side surfaces of TDO and NDO samples are shown in Figure 3.3 to support the content of deformation maps in Figure 3.2. Note that in Figure 3.3, left and right columns indicate $TD^{\perp}$ (TDO-top and NDO-side) and $ND^{\perp}$ (NDO-top and TDO-side) surfaces. The reason of plotting histograms of identical material (plate) planes is to show statistical coherence of data in both samples. The statistical equivalence of two specimens will be discussed at the end of this section.

Top surface of TDO sample (i.e. TD-normal face) does not exhibit distinct localization features up to load point c. Starting with point c, certain localization features show in the axial strain maps. This macroscopic strain localization exhibits a homogenizing trend in the next load (see point d). The relative homogeneity of the TDO macro-top strain field is also noticed in Figure 3.3 first column. The increase in overall

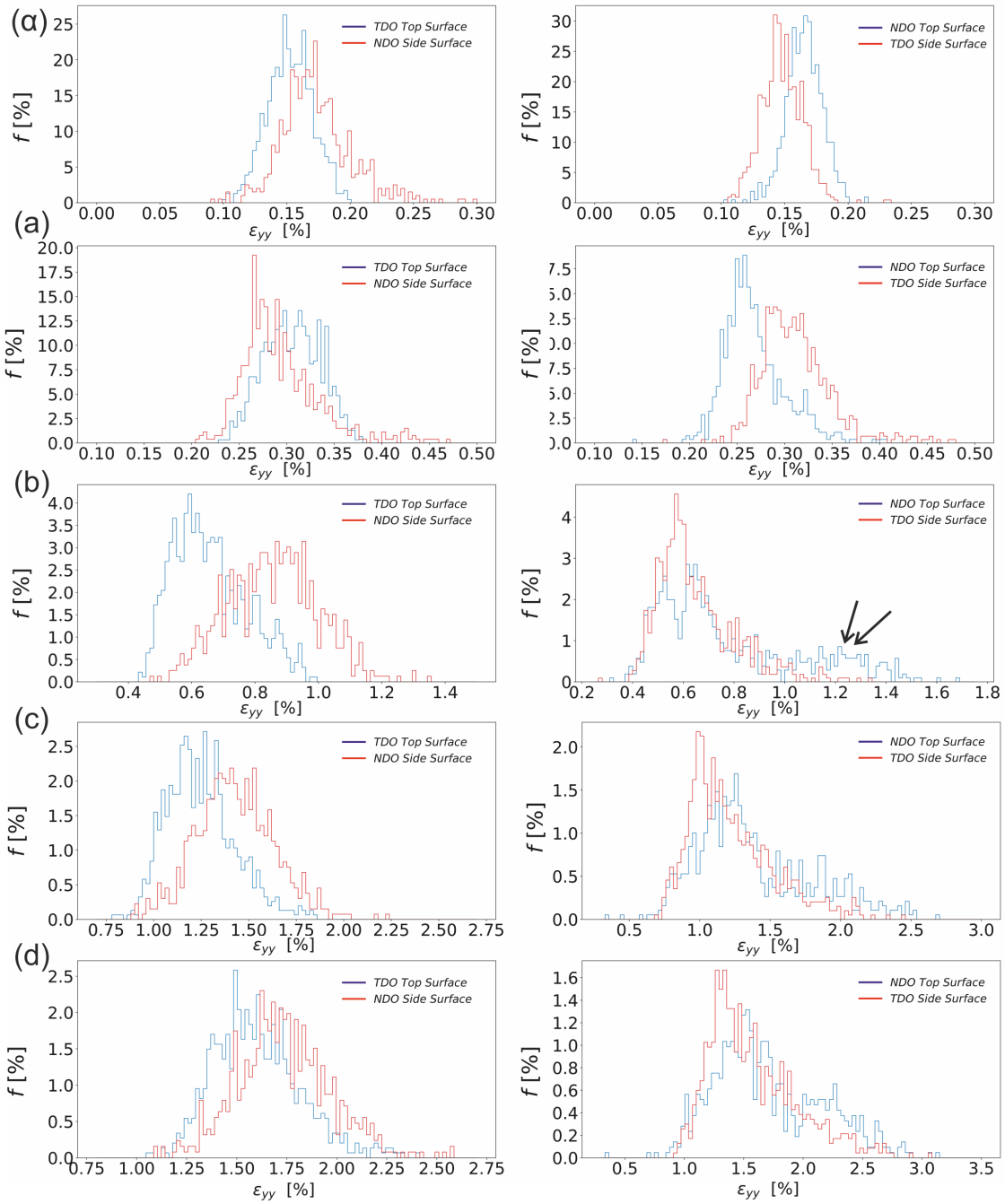

Figure 3.3. εyy histograms of top and side faces of TDO and NDO specimens.

strain of TDO top surface does not proceed with a growing $\|\delta\varepsilon_{yy}\|$ / $\bar{\varepsilon}_{yy}$ axial strain value (see also Table 3.1).

In contrast, on the top face of NDO macro-field, thick horizontal bands of strain heterogeneities emerge at point b (Figure 3.2, second row). In the right column of Figure 3.3, the appearance of horizontal patterns of heterogeneities can also be observed as a weak second peak (shown by arrows) on the NDO-top histogram of point b. As visual intensity of horizontal strain heterogeneities increases at point c and d, strain content and relative data frequency of such statistical populations also increase as shown in Figure 3.3. The overall impact of the heterogeneity resulting from horizontal bands is evident on ND-normal face histograms; noting the considerably greater strain span in comparison to the TDO top face. The clear contrast on the orthogonal faces of the Magnesium AZ31 plate reveals the anisotropic nature of the material regarding both localization character and heterogeneity of strain.

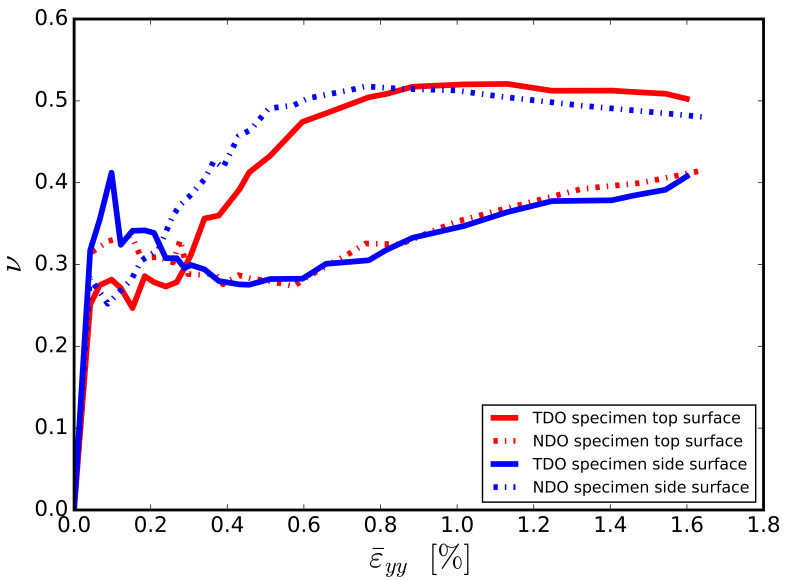

Figure 3.4. In-plane Poisson's ratio of TDO and NDO samples.

Similar conclusions can also be drawn on Figure 3.4. In this figure, effective poisson's ratio ν of top and side surfaces of TDO and NDO specimens are plotted versus average strain. In-plane ν of TD and ND surface is around 0.3 in elastic regime, after the transition TD plane reaches an average ν of 0.5 whereas ND face maintains the low ν value (between 0.3 and 0.4) with increasing strain. This trend also validates the anisotropy of RD-tensioned Mg in early plastic region. In the reverse load, anisotropy

due to profuse twinning is even more pronounced. Kapan *et al.* [14] show a trend toward $\nu = 1$ on TD and $\nu = 0$ on ND surface. However, in the absence of profuse twinning activity the material shows a less extreme plastic behavior in a macroscopic sense. This is only one of the many indicators of the the stong tension-compression anistropy of sharply-textured rolled Magnesium.

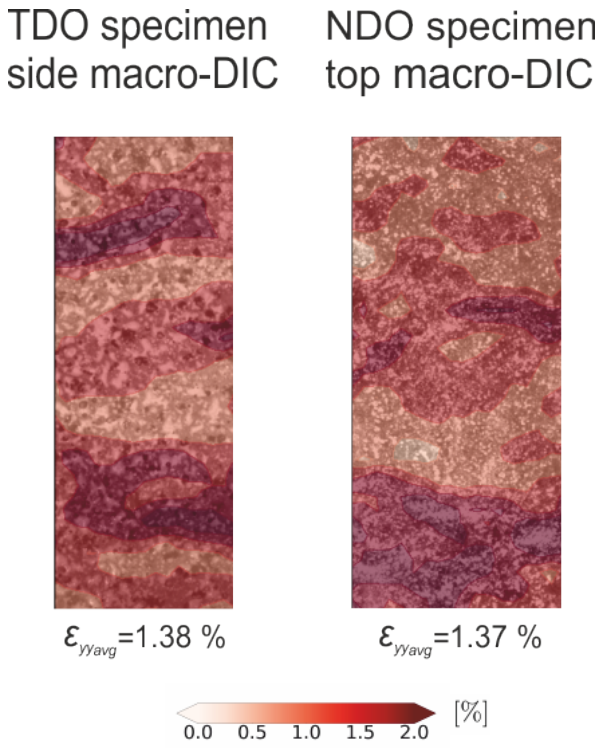

Figure 3.5. ε_{yy} field of NDO top and TDO side surfaces at 1.37 % average strain

In order to make a solid interpretation on volumetric deformation behavior of RD-tensioned material, agreement of the two samples should be ensured in a statistical sense. To corroborate the statistical equivalence, Poisson's ratio of side surface of both TDO and NDO specimens is also presented in Figure 3.4. Apart from small deviations, the two effective-ν curves measured over RD-ND material plane (TD-normal plane), namely, TDO-top and NDO-side measurements, agree. A similar statement holds for curves measured over RD-TD material plane (ND-normal plane), namely NDO-top and TDO-side, observations.

The compatibility of TD-normal and ND-normal planes of both specimens is noted on the histograms, Figure3.3 as well. In the left column of Figure 3.3, TDO-top and NDO-side (i.e. $TD^{\perp}$ plane) histograms show a close span though their average strain varies slightly (expected from the slight variations in strain points of the two samples). Similar observation can also be made on histograms of NDO-top and TDO-side ($ND^{\perp}$ plane). Additionally, for $ND^{\perp}$ plane, heterogeneity pattern starting from point b presents a strong coherence among NDO-top and TDO-side faces. Hence, TD and ND-normal planes shows quite similar quantitative behavior of strain heterogeneity in both specimens. In addition to quantitative similarity of both samples, spatial consistency of TDO and NDO strain patterns can be noted in Figure 3.5. Macro-DIC strain maps of TDO-side surface and NDO-top surface at 1.35% of strain show the similar near-horizontal bands of strain localization. Though band patterns of both $ND^{\perp}$ faces do not exactly match as expected from the stochastic nature strain localization, the characteristics of deformation pattern is equivalent.

3.2. Mesoscale observations

3.2.1. Combination Maps

Figure 3.6 and 3.7 show the micro-DIC combination maps of the gage section area (as described in section 2), depicting entire macroscopic fields with microstructural resolution. Axial strain ε_{yy} and rotation ω_{xy} results for TDO an NDO samples are plotted side by side for each stage of deformation, indicated with a-d standing for equivalent load points. The very first micro-DIC load point, α shown in Figure 3.1, only show flat bands over the TDO field that are hardly discernible in the full-field presentation of 3.6 (see Appendix A for all deformation stages). Therefore, these will rather be exemplified in Section 3.3 over local region of interest maps.

At load stage a (Figue 3.6(a)) that nearly marks the onset of clearly observable plastic activity, the dominant strain localization structures on the TDO face are thin, near horizontal bands. The precursors of these has been observed at point α. However,

at point *a*, strain localization in the form of non-45° bands -not present at stage α- also emerge at few localities. Over the NDO field, low angle flat bands accommodate the strain, but there is no sign of strain localization in the form of non-45 bands. No prominent pattern is discernible on the rotational field of both faces at this loading stage. The origin of indistinct traces underlying non-45° bands (TDO map) becomes clear at the next load stage.

At stage *b* Figure 3.6 , non-45° bands of strain localization clearly gain prominence over the TDO surface. The number of non-45 bands increase and their occurrence homogenizes over the gage section. Along with the intensifying non-45° bands, the strain content of the flat localization structures also increase with respect to stage *a*. The main utility of presenting rotation maps in this study, namely, shedding light on orientations of simple shear processes, becomes apparent at this point: Over 3.6 TDO rotation (ω_{xy}) map, only the $\pm\theta$ families of non-45° bands are present (with senses consistent with Figure 2.6(a)), whereas flat localization structures in the ε_{yy} map are filtered out. This suggests that the plane of shear of the flat localization structures should be near orthogonal to the observation surface x-y (Figure 2.6(d)) while the plane of shear of pm theta structures should have a high degree of alignment with x-y. On the other hand, the deformation patterns over the orthogonal NDO maps are distinctly different as there is clearly no sign of the non-45° bands. Rather, the horizontal band structures intensified and coalesced with respect to the previous stage *a*; and on the ND surface the stage-*b* rotation map does not show any strong indication of individiual simple shear process as captured on non-45° bands. Instead, scarcely noticable ±45° rotation pattern appears.

Through stages *c* and *d* (Figure 3.6), the presented spatial features intensify on both TDO and NDO surfaces but do not significantly change character. Non-45° bands as well as the remaining structures on the background keep accommodating further strain over the TDO maps. The non-45° structures over the TDO map can be called mesoscale structures, since, they are not individually observable (largely averaged out, Figure 3.2) over the macro-DIC maps (Section 3.1). NDO strain maps, on the

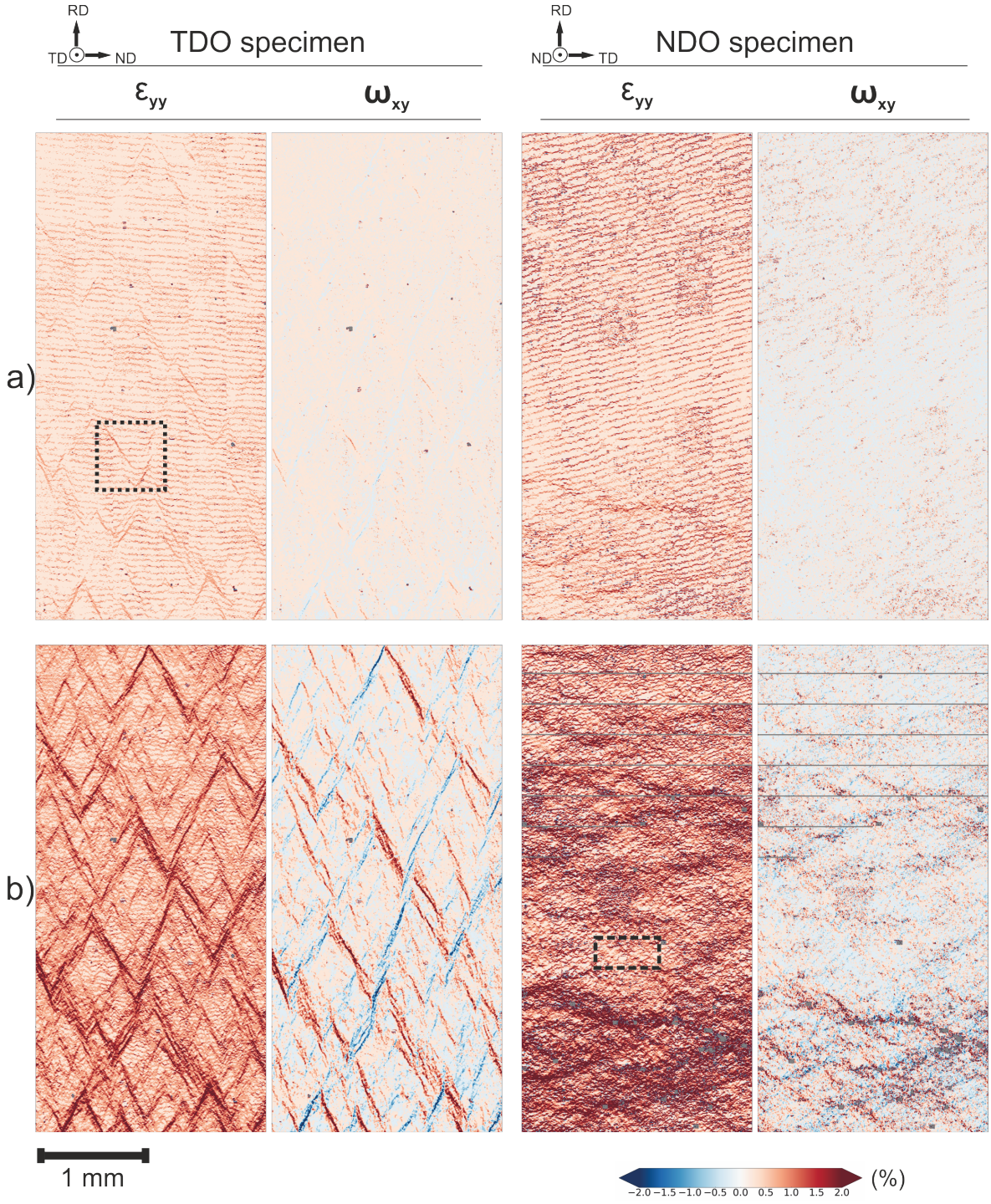

Figure 3.6. Full size micro-DIC combination maps of load point a and b for axial strain (ε_{yy}) and rotation (ω_{xy}) for both TDO and NDO samples plotted side by side at equivalent stages

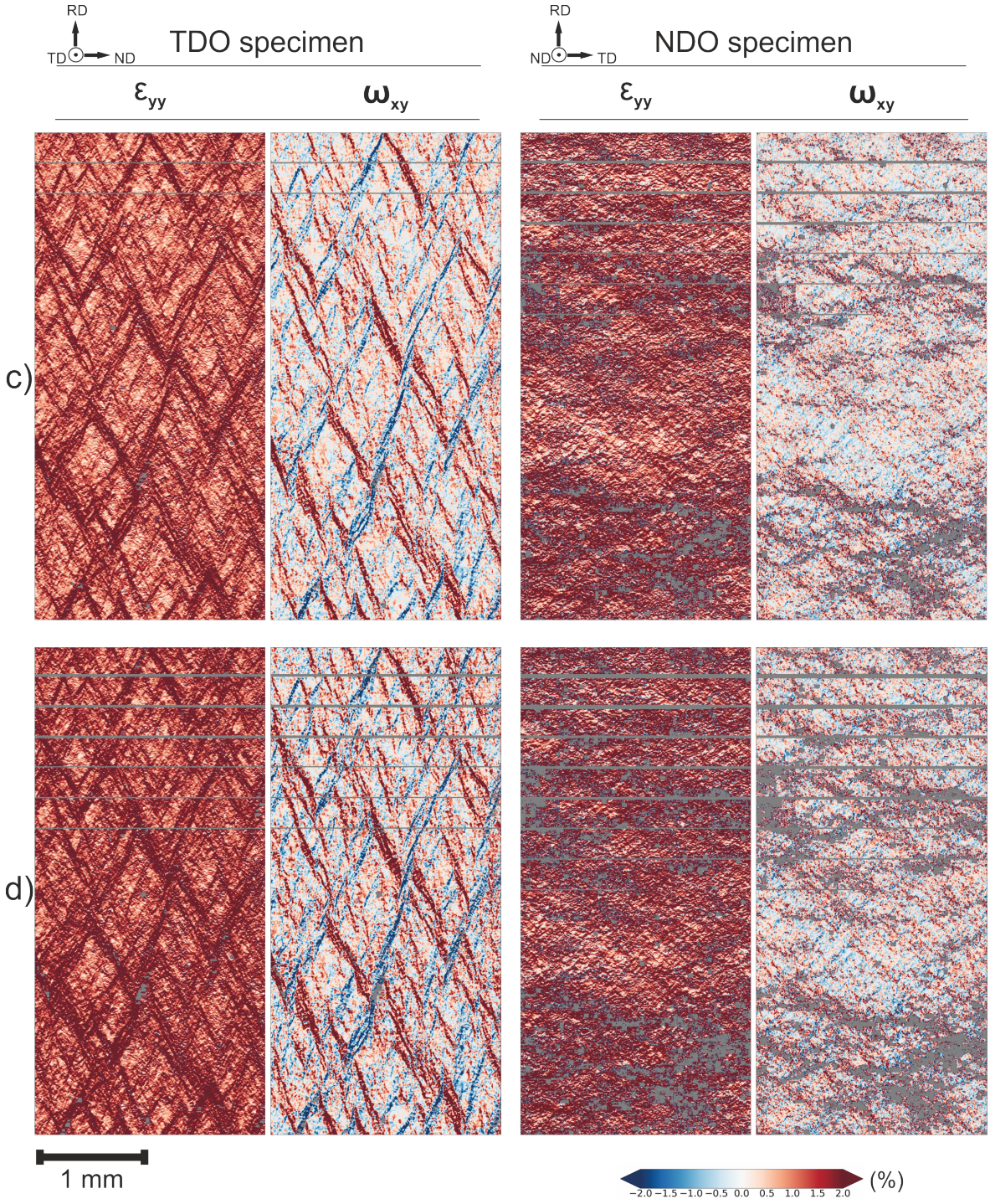

Figure 3.7. Full size micro-DIC combination maps of load point c and d for axial strain (ε_{yy}) and rotation (ω_{xy}) for both TDO and NDO samples plotted side by side at equivalent stages

other hand, cease to show any distinctly-identified band structures at the micro-DIC resolution. They, however, show horizontal strain localizations at a larger scale that are also observable over the macro-DIC maps in Section 3.1. Particularly over these high-strain regions, DIC invalidations become prominent on the NDO maps over load stages *c* and *d*, indicating intense roughening on the ND surface. Besides, outside the regions of strong invalidations due to out-of-plane deformation activity, the slight rotation pattern arising at stage *b* intensifies at later satges of defotmation. The aspects of this pattern will be discussed in detail with further quantitative results in section 3.3.

3.2.2. Statistical evaluation

Table 3.2. Micro-DIC average axial, transverse strain and the respective strandard deviation values of TDO and NDO samples

(%)	TDO				NDO			
	$\bar{\varepsilon}_{yy}$	$\|\delta\varepsilon_{yy}\|$	$\bar{\varepsilon}_{xx}$	$\|\delta\varepsilon_{xx}\|$	$\bar{\varepsilon}_{yy}$	$\|\delta\varepsilon_{yy}\|$	$\bar{\varepsilon}_{xx}$	$\|\delta\varepsilon_{xx}\|$
α	0.144	0.155	-0.038	0.148	0.162	0.371	-0.044	0.328
a	0.31	0.203	-0.098	0.185	0.272	0.474	-0.071	0.405
b	0.671	0.702	-0.331	0.428	0.743	1.008	-0.234	0.849
c	1.228	0.816	-0.617	0.837	1.239	1.937	-0.542	1.626
d	1.572	1.108	-0.765	1.115	1.442	2.431	-0.74	2.023

Table 3.2 shows average strains, $\bar{\varepsilon}_{yy}$, $\bar{\varepsilon}_{xx}$ of TDO and NDO sample with the respective standard deviation ($\|\delta\varepsilon_{yy}\|$, $\|\delta\varepsilon_{xx}\|$), this time calculated from the micro-DIC field with over 3 million data points for each load. This allows much higher-statistical signifance, and smoother histograms plotted in 3.8 for both samples compared to macro-scale distributions of Fig.3.3. Resolved strain heterogeneity is length scale-dependent and over the same material fields, this means much wider histograms and larger standard deviations for the meso-scale measurement (3.2), compared to the macro-scale measurement (see Table 3.1).

On the other hand, averages should agree regardless of the measurement length scale. For the TDO sample, $\bar{\varepsilon}_{yy}$ and $\bar{\varepsilon}_{xx}$ values of the micro-DIC measurement shows a good agreement with macro-top average strains. However; for NDO sample invalidations over thick horizontal, as also observed especially at point c and d in Figure 3.7, cause $\bar{\varepsilon}_{yy}$ to stray from average strain value at macroscale (max. difference is around 17 %) simply due to loss of data at some high-strain neighborhoods.

The significant difference observed in macroscopic histograms of TDO and NDO samples (Figure 3.3) also reflect in the mesoscale measurement (Figure 3.3). As quantified over Table 3.2, strain heterogeneity on NDO field is remarkably greater. Precisely, $\delta\varepsilon_{yy}$ and $\delta\varepsilon_{xx}$ values over NDO are more than twice of the corresponding values over the TDO field. Spatially, TDO field shows a more homogeneous strain distribution which can be noticed in the regular intervals of strain localization structures through loads *a*-*d*, shown in Figure 3.6 and 3.7.

An important aspect on TDO histograms is that, starting from point b, ε_{yy} and ε_{xx}, histograms both exhibit a sharp drop while approaching to zero. This behavior steering away from the symmetry of a typical Gaussian distribution points to the presence of strain heterogeneity patterns. To investigate this point, histograms of non-45° bands are plotted separately at point b by employing $\pm$ 1 % ω_{xy} data filtering (explained in detail in Section 3.3.2). As can be observed in TDO non-45° histogram 3.8, the high-strain tails of the field histograms that break the symmetry are rooted in the emergence of non-45° shear bands.

An even more notable irregular distribution is evident on NDO histograms. At point b, a hump arises around 1 % axial strain (shown by arrows) on ε_{yy} histogram which indicates that overall ε_{yy} histogram contains strain populations from two distinct structures. To distinguish one of the populatins, histogram of a selected box in a low strain region (Figure 3.6) is plotted. The coherence between sharp peak of point b NDO and total histogram of NDO selected box is clear. Therefore we can conclude that the hump that contains greater and more heterogeneous strain content stems from the

macroscopic strain localization bands. The hump that emerges at point b comes closer to the sharp peak at each loading stage (again shown by arrows). This is consistent with the spatial observation that thick horizontal strain localization spread over the field at later stages of plasticity (also see Figure 3.7).

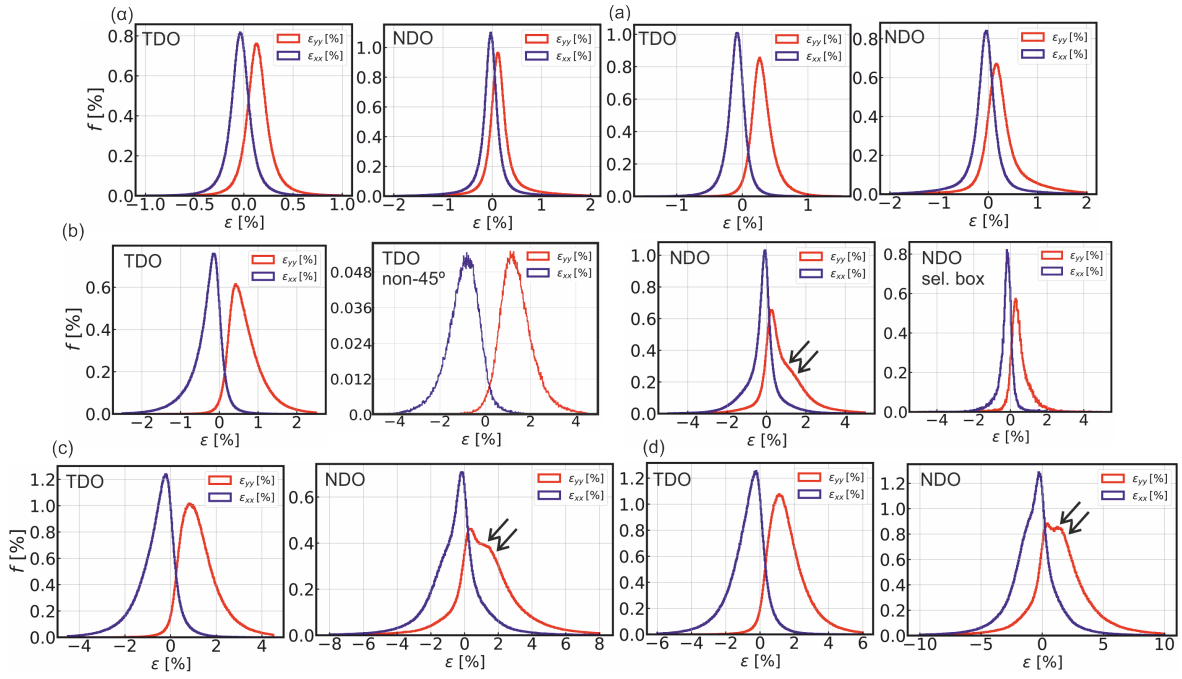

Figure 3.8. Mesoscale ε_{yy} and ε_{xx} histograms of TDO and NDO samples

Based on mesoscale results of Figure 3.6, 3.7, 3.8 and Table 3.2 it can be concluded that the vast difference between the deformation characteristics of TDO and NDO samples, effectively representing deformation over TD and ND planes of an RD-loaded sample, show the very high level of plastic anisotropy evident in these materials. Here though, on top of the macroscopic understanding in the literature (typically put in terms of the r-ratio [9, 41]), multi-scale strain heterogeneity is characterized quantitatively.

3.3. Quantification of localization structures

3.3.1. Individual Poisson's Ratio Map

Rotation (ω) and Poisson's ratio (ν) are adequate parameters to identify in-plane ($\nu = 1$) and out-of plane ($\nu = 0$) shear activities on planes of interest as discussed in Section 2.4. Utilising these variables, it is intended to describe quantitative (and consequently physical) nature of flat and non-45 $^\circ$ localization structures of the TDO sample as well as the early deformation patterns on NDO sample. First approach to characterize the localization structures is to use individual Poisson's ratio (ν^{ind}) as a filtering parameter. As presented in Equation 3.1, ν^{ind} is collected at each material point as a new variable over the deformation field, then by averaging out ν^{ind} (Equation 3.2) over the entire DIC area $\bar{\nu}^{ind}$ is obtained.

$$\nu^{ind} = -\frac{\varepsilon_{xx}^{ind}}{\varepsilon_{yy}^{ind}} \tag{3.1}$$

$$\bar{\nu}^{ind} = \overline{\left[-\frac{\varepsilon_{xx}^{ind}}{\varepsilon_{yy}^{ind}}\right]} \tag{3.2}$$

$\bar{\nu}^{ind}$ is here employed as a limiting variable for flat and non-45 $^\circ$ structures of TD-normal face. Flat bands are high strain localization structures with no rotation pattern whereas non-45 $^\circ$ bands show a strong $\pm\theta$ rotation content as depicted in Figure 3.6 (a) and (b). As a consequence, flat and non-45 $^\circ$ bands are expected to possess relatively low and high ν respectively. To perform an investigation on the content of both type of strain localization the following filtering operation is utilized: Data points having lower ν^{ind} than $\bar{\nu}^{ind}$ are plotted for flat bands in Figure 3.9(a). In a similar manner, to observe non-45 $^\circ$ bands separately points with greater ν^{ind} (i.e. ν^{ind} $\bar{\nu}^{ind}$) are portrayed

in Figure 3.9(b). Additionally, the histograms plotted next to ν^{ind} maps show the ν^{ind} distribution over the related combination maps of 3.9(a) and (b). Note that (a) and (b) categorization of Figure 3.9 also refers to load point a and b of TDO sample. The reason of using alternate load points to demonstrate each type of localization patterns is their dominance on the deformation field at the corresponding load points. Namely, flat bands are evidently prevalent strain localizations apart from few early non-45° bands at load point a while load point b is the stage of deformation where non-45° bands form the prominent character of the entire map.

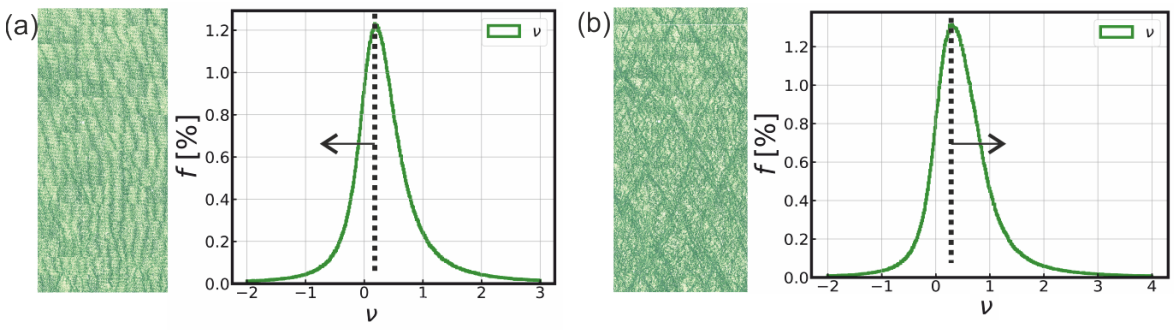

Figure 3.9. ν^{ind} map and corresponding histograms at load point a and b

On filtered-ν^{ind} map of load point a (Figure 3.9(a)), it can be seen that targeted horizontal bands could be distinguished as intended. However; the overall pattern seems to also organize in some vertical localization structures. As observed in Figure 3.9(a) ν^{ind} smaller than 0 has a considerable distribution on the corresponding histogram. Therefore the negative ν^{ind} content unsurprisingly appears on the combination map with extreme contrast since coloring of the contour map is produced within the interval of ν^{ind}=0 (dark green) and ν^{ind}= $\bar{\nu}^{ind}$ (white). The vertical bands typically stem from ε_{xx} localizations that will be presented in the next section (Figure 3.13-(a)).

Figure 3.9(b) operation to distinguish non-45° bands indeed selects these structures. Yet, the structures in between the prominent non-45° bands also appear on the combination map (see Figure 3.9-(b)). Similar to the observations on histogram (a), extreme ν^{ind} content (simply greater than 1) also takes place in the non-45° band filtering. Consequently; the Poisson's ratio filtering does no single out non-45° as

sharply as desired (as observed in Figure 3.6-(b)).

A clear complication in dealing with pointwise Poisson's ratio filtering is the content that remains outside the Poisson's ratio limits that are defined for the nominal stress state (uniaxial stress along y). For this stress state, sensible values of Poisson's ratio falls between $0 < \nu < 1$ (Section 2.4). The off-limit content ($\nu < 0$ and $\nu > 1$)points to local stresses that significantly deviate from the nominal stress state. This puts limits on ν^{ind}-filtering in targeting individual mesoscale structures. Here, ω and ε filtering have been found to be more conducive for this aim.

3.3.2. Flat and non-45° bands on TDO sample

Outlier ν^{ind} content on filtering maps causes a distraction to produce a physical interpretation on strain localization patterns. Therefore, based on the nature of rotation maps of the TDO sample presented in Figure 3.6 and 3.7, ω_{xy} is utilized as the primary parameter to filter out the targeted localization structures.

As mentioned in the previous subsection, load point a is the most relevant stage to isolate flat bands. Flat bands are simply high strain regions and the filtering operation involves separating the data points whose ε_{yy} value is greater than a specific ε_{yy}^{lim}. Then overall $\nu(\varepsilon_{yy}^{lim})$ of the filtered regions is calculated as described in Equation 3.3 . For statistical significance, area fraction (AF(ε_{yy}^{lim})) of the filtered points is defined in Equation 3.4. This variable is presented to check the remnant fraction of the localization structure as a function of the applied limit.

$$\nu(\varepsilon_{yy}^{lim}) = \frac{-\bar{\varepsilon}_{xx}(\varepsilon_{yy} > \varepsilon_{yy}^{lim})}{\varepsilon_{yy}(\bar{\varepsilon}_{yy} > \varepsilon_{yy}^{lim})} \tag{3.3}$$

$$AF(\varepsilon_{yy}^{lim}) = \frac{N(\varepsilon_{yy} > \varepsilon_{yy}^{lim})}{N_{total}} \tag{3.4}$$

Imposed over the above filter, the limited content of non-45 $^\circ$ bands at point a is eliminated using the additional low-rotation filter (ω_{xy}) filter of 0.1 %. Then, starting from the ε_{yy} limit of average strain of the overall field (0.31 %), strain limit is stepwise pulled up to twice the average strain (0.62 %). Table 3.3 shows the ε_{yy}^{lim} at each filtering step and corresponding average ε_{yy} and ε_{xx} of the filtered material points, ν and area fraction. Utilising the data from Table 3.3, the chart showing ν and area fraction trends with ascending ε_{yy}^{lim} is created (see Figure 3.10). For visual representation of isolated flat bands, the related binary maps are plotted at two exemplified limiting steps marked with '■' and '★'). Here black refers to the selected point. Note the white traces over non-45 $^\circ$ structures that imply their successful elimination.

Table 3.3. Average ε_{yy} and ε_{xx}, ν and area fraction percentages of flat bands at each ε_{yy}^{lim}

ε_{yy}^{lim} (%)	$\bar{\varepsilon}_{yy}$ (%)	$\bar{\varepsilon}_{xx}$ (%)	ν	Area Fraction (%)
0.311	0.444	-0.0832	0.1875	28.58
0.388	0.5219	-0.0823	0.1578	15.70
0.466	0.6070	-0.0792	0.1304	8.51
0.544	0.6948	-0.0750	0.1079	4.65
0.622	0.7849	-0.0688	0.0877	2.61

As ε_{yy}^{lim} increases average ε_{xx} of separated region decreases with increasing positive strain. As a consequence average ν of the masked area decreases at each step as observed in Table 3.3. The typifying filter maps shown in Figure 3.10 disclose that the intensity of flat structures weakens with decreasing average ν. At the final step of the limit range, it is observed that the average Poisson's ratio goes down to 0.08 with still considerable amount of area fraction (around 3 % meaning 1x10^5 points. This small quantity of ν approaching to zero means that the collaborative shear activity in flat

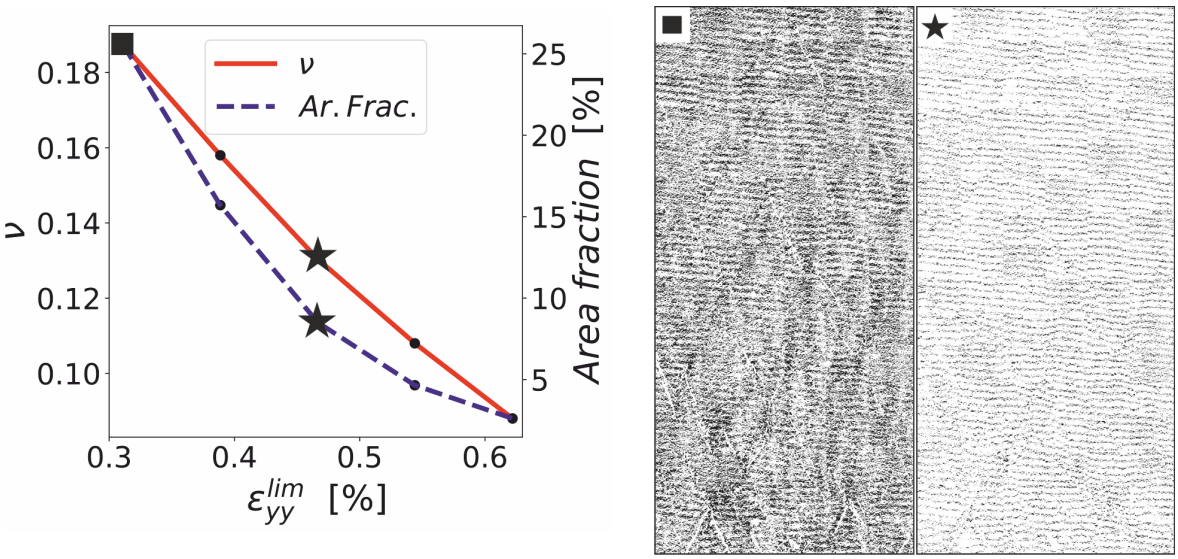

Figure 3.10. ν and area fraction vs ε_{yy}^{lim} and representative binary filter maps of flat bands

localization structures is basically out of plane.

In contrast, non-45 $^\circ$ bands are strongly associated with ω_{xy} patterns. Therefore, absolute ω_{xy}^{lim} is used to single out non-45 $^\circ$ structures at load point b. This absolute limit excludes data points within the interval of $\pm\omega_{xy}$ and presents high rotation regions. Thus, out-of-plane flat structures are clearly masked to reveal non-45 $^\circ$ bands. Additionally, the ω_{xy} range is gradually confined so that regions of intense shear activity can be observed. Equation 3.5 and 3.6 is derived in a similar manner to find average ν and area fraction of this strong shear structures. Table 3.4 demonstrates once again average ε_{yy} and ε_{xx} of the filtered material points, ν and area fraction of the filtered region with increasing ω_{xy}^{lim}.

$$\nu(\omega_{xy}^{lim}) = \frac{-\bar{\varepsilon}_{xx}(|\omega_{xy}| > \omega_{xy}^{lim})}{\bar{\varepsilon}_{yy}(|\omega_{xy}| > \omega_{xy}^{lim})} \tag{3.5}$$

$$AF(\omega_{xy}^{lim}) = \frac{N(|\omega_{xy}| > \omega_{xy}^{lim})}{N_{total}} \tag{3.6}$$

Table 3.4. Average ε_{yy} and ε_{xx}, ν and area fraction percentages of flat bands at each ω_{xy}^{lim}

ω_{xy}^{lim} (%)	ε_{yy}^{-} (%)	ε_{xx}^{-} (%)	ν	Area Fraction (%)
(-1,1)	1.3786	-0.9825	0.712	5.71
(-1.25,1.25)	1.5440	-1.1532	0.747	3.21
(-1.5,1.5)	1.7130	-1.3070	0.771	1.85
(-2,2)	1.9838	-1.6121	0.813	0.69
(-2.5,2.5)	2.2067	-1.8717	0.848	0.29

Figure3.11 shows average ν trend of the filtered structures (with corresponding area fractions) that are gradually confined to higher rotations by increasing ω_{xy}^{lim}. The examplifying masked maps (marked with square and star) belong to first and third stage of filtering, plotted next to ν trend chart in Figure3.11. At 1 % of ω_{xy}^{lim}, non-45° bands covering 6 % (18x10^4 data points) of overall area have average ν of 0.712. As the rotation is further limited, average ν increases and non-45° bands narrow down to their core. This indicates higher degree of in-plane shear activity at the center of each individual non-45° band. High-ν content in the bands at each mask step imply that the shear activity associated with the non-45° bands is largely in-plane.

3.3.3. Localizations on NDO sample

The mesoscopic localization patterns on NDO sample are difficult to distinguish (unlike TDO), particularly after load point *b* where the fields segregate macroscopically. Only load-point *a* near flat bands (hereafter these structures are called ND-flat bands to avoid confusion with flat structures over the TDO sample) in Figure 3.6 (a) can be targeted unambiguously by full-field filtering. Similar to the condition of flat band filtering of TDO specimen, Equation 3.3 and 3.4 are used to separate high strain locales.

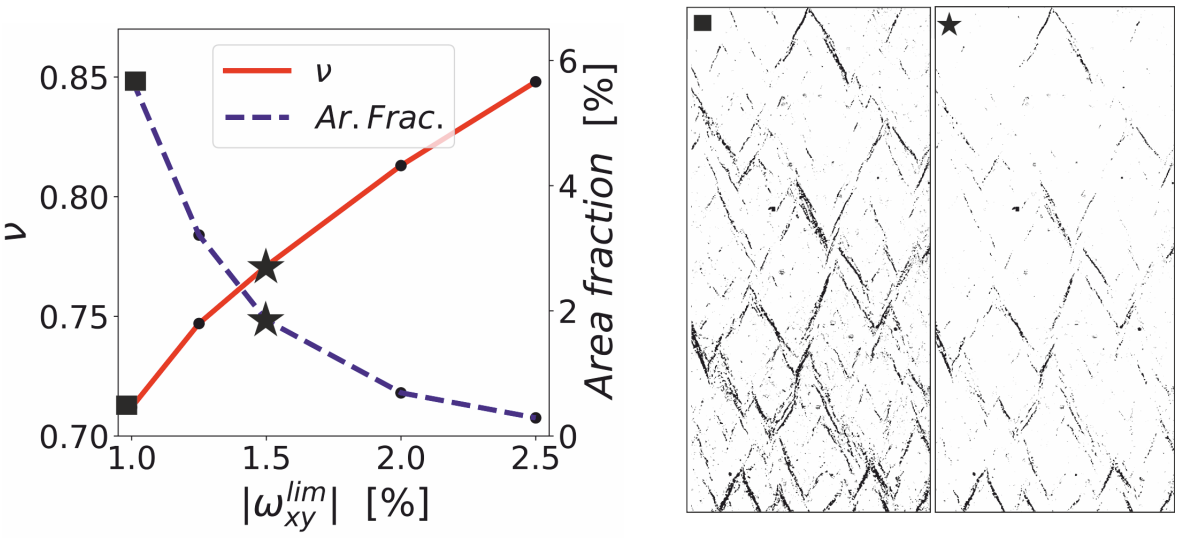

Figure 3.11. ν and area fraction vs ω_{xy}^{lim} and representative binary filter maps of non-45° bands

As shown in Figure 3.7 (a) ω_{xy} of NDO sample, no intense rotation content is noticed on the combination map. Thus, constant rotation filter range is not introduced in this case. Table 3.5 shows average ε_{yy} and ε_{xx}, ν and area fraction percentages of high strain structures with increasing ε_{yy}^{lim}. Compared to flat structures of TDO field, localization patterns of the ND face at point a have greater positive axial strain content (on average, around 2.5 times of ε_{yy}^{lim}) with slightly smaller magnitudes for transverse strain, ε_{xx}. Consequently, average ν of ND-flat structures are considerably small than the bands of TDO sample. More clearly, at each limiting step average ν (ranging between 0.077-0.036) is practically zero and the structures can be regarded purely out-of-plane.

The statistical significance of ND-flat bands is also presented on the last column of Table 3.5 as well as in Figure 3.12. Imposing more strict limits on ε_{yy}^{lim} does not generate a dramatic drop on data fraction as observed on flat bands of NDO sample. Doubling the limit decreases the area fraction of ND-flat bands from 40 % to 18 % whereas the portion of flat localizations on TD face drops down to almost one tenth-of its original content (28.52 %, see Table 3.3). The predominance of ND-flat bands can

Table 3.5. Average ε_{yy} and ε_{xx}, ν and area fraction percentages of flat localizations on NDO sample at each ε_{yy}^{lim}

ε_{yy}^{lim} (%)	ε_{yy} (%)	ε_{zz} (%)	ν	Area Fraction (%)
0.283	0.708	-0.054	0.077	39.26
0.354	0.810	-0.051	0.064	31.16
0.425	0.911	-0.048	0.052	25.19
0.496	1.005	-0.044	0.044	20.83
0.566	1.092	-0.039	0.036	17.59

also be observed on binary maps of Figure 3.12.

At the bottom of the gage section, confining ε_{yy}^{lim} does not present a pure selection of ND-flat bands. Rather the precursors of the second-wave of segregated bands (that will intensify over points *b*-*d*), superimpose over the ND-flat bands (see the transition between binaray maps '■' and '★'). Still, the low ν for all heterogeneities indicates that collaborative movement of deformation is out-of-plane shear activity on ND-face.

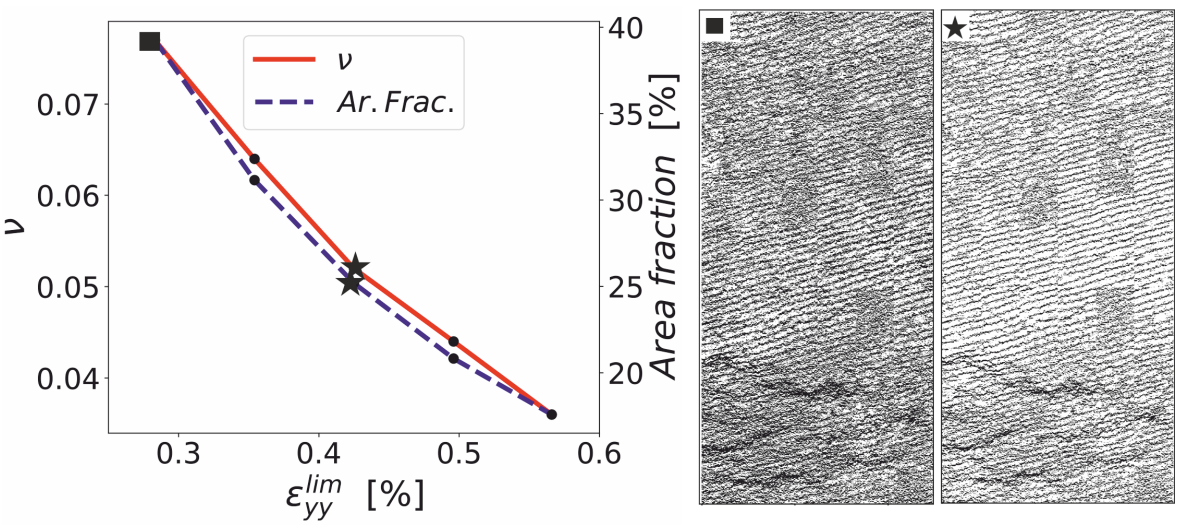

Figure 3.12. ν and area fraction vs ε_{yy}^{lim} and representative binary filter maps of localization structures of NDO sample

Another notable quantification for NDO sample is the content of the box selected on Figure 3.6(b) in the low-strain belt. As emphasized in Figure 3.8 of Section 3.2, the additional hump emerging at load b stemmed from the second wave of segregated heterogeneity patterns that are also visible at macro-scale. To show the minor strain content of the rest of the entire region, axial strain distribution of the representative selected box is plotted in Figure 3.8. The separated histogram reasonably matches with the main peak of histogram point b of NDO sample and average ν of the box is around 0.6 as deviating from overall ν. In fact; the indication of relatively higher ν can be noticed from ω_{xy} combination map. Vague ± 45 ω_{xy} pattern points out the considerable in-plane shear activity in the representative region of the selected box. Although the box is taken from low strain region, the influence of strain localization of horizontal bands is non-negligible here. In order to optimize low axial strain area selection, a complex geometry filter mask (not shown) that negotiates between flat shear localization traces, is prepared. The resultant ν over such a region can be as high as 0.7 which indicates relatively strong in-plane shear activity over the NDO face compared to the rest of the field.

3.4. Morphological assessment of localization structures

Figure 3.13 demonstrates the evolution of the box (600 x 600 μm^2) taken from TDO field (see Figure 3.6) with α-d load stages. Overlaying ε_{yy} and ε_{xx} fields with 0.5 transparency of are presented to associate strain localization structures with surface morphology. It is noteworthy to mention here that such operation for NDO field is not included here due to the following reason: Neither morphology of ND surface nor related localization structures have severely distinguishable nature. The necessary interpretations regarding the characteristics of strain localizations of NDO sample will be made in Section 3.4 with further quantitative observations.

For illustrative purposes point a is selected for the representation with greater size since strain heterogeneities in the form of non-45° and flat bands are present here with a strong contrast. The rest of the load points are sorted in ascending order based

on their individual average strain value. Similarly, colorbar on the top of each frame adjusted according to the corresponding average ε_{yy} and ε_{xx} values to facilitate the visual comparison.

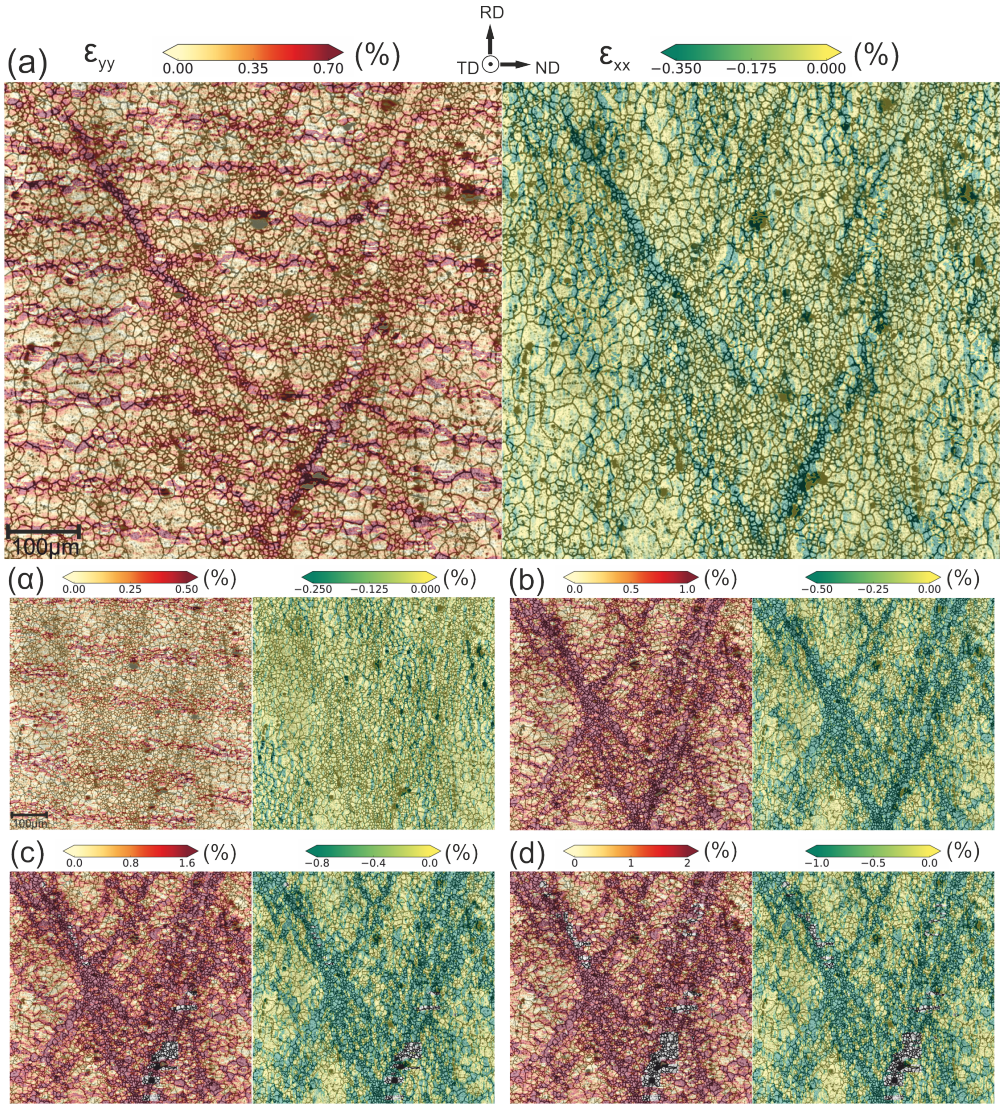

Figure 3.13. ε_{yy} and ε_{xx} of a selected box taken from TDO field.

Before getting into further detail on deformation fields associated with the microstructure, it is crucial to mention the characteristics of TD face morphology to construct a solid base for discussion. As can be noted on Figure 3.13(a); the microstructure has an obvious bimodal character. More specifically, there are distinct collections of smaller grains that form microstructure bands with 60° angle with the horizontal. The rest of field lies outside the network of these microstructure bands is occupied with relatively large grains.

Starting point α, as emphasized in Section 3.2, subtle horizontal flat bands of strain localization structures for ε_{yy} are prominent in the selected box. However, no similar structure can be captured for ε_{xx} field; rather localization structures have tendency to accumulate in the form of vertical inhomogeneous patterns. These initial localization structures of axial and transverse strain has no particular correlation with the bimodal morphological picture at this stage of deformation.

In the following load point (point a), flat bands arising at point alpha condense and becomes thinner over ε_{yy} field. In addition to flat band localization structures, non-45° band structures show up. In fact, this angled strain localization structures exhibit a perfect coincidence with underlaying microstructure observed in Figure 3.13(a). Non-45° strain heterogeneities at both ε_{yy} and ε_{xx} field localizes on relatively small grain aggregates. However; it should be noted that the bimodal strain pattern captured on ε_{yy} field of load point a is not observed on ε_{xx} picture. Instead, strain localization individually shows itself as non-45° bands. In fact, as discussed in Section 3.3.2, this is another indication of in-plane shear activity in non-45° bands with strong ε_{yy} and ε_{xx} content.

At load point b, non-45° strain localizations gain prominence on the deformation field over flat bands as also indicated in Figure 3.6. Pre-existing non-45° bands expand and further bands emerges over relatively small grain clusters (see Figure3.13(b) bottom-left and middle-left). As a consequence, visibility of flat bands weakens over the interested region. The same characteristic propogation (growth of non-45° bands)

with an obvious decelaration is also noticed on ε_{yy} field of point c and d. During the evolution of non-45° bands after point a, it is observed that the growth of these bands is typically confined within the extent of small grain aggragates. This strong morphological dependency of strain localization signifies inherent microstructural heterogeneity of the material. Another notable interpretation regarding the association of localization structures with morphology is the presence of flat bands over relative large grains as being links between non-45° bands(undetectable at point c and d of Figure 3.7).

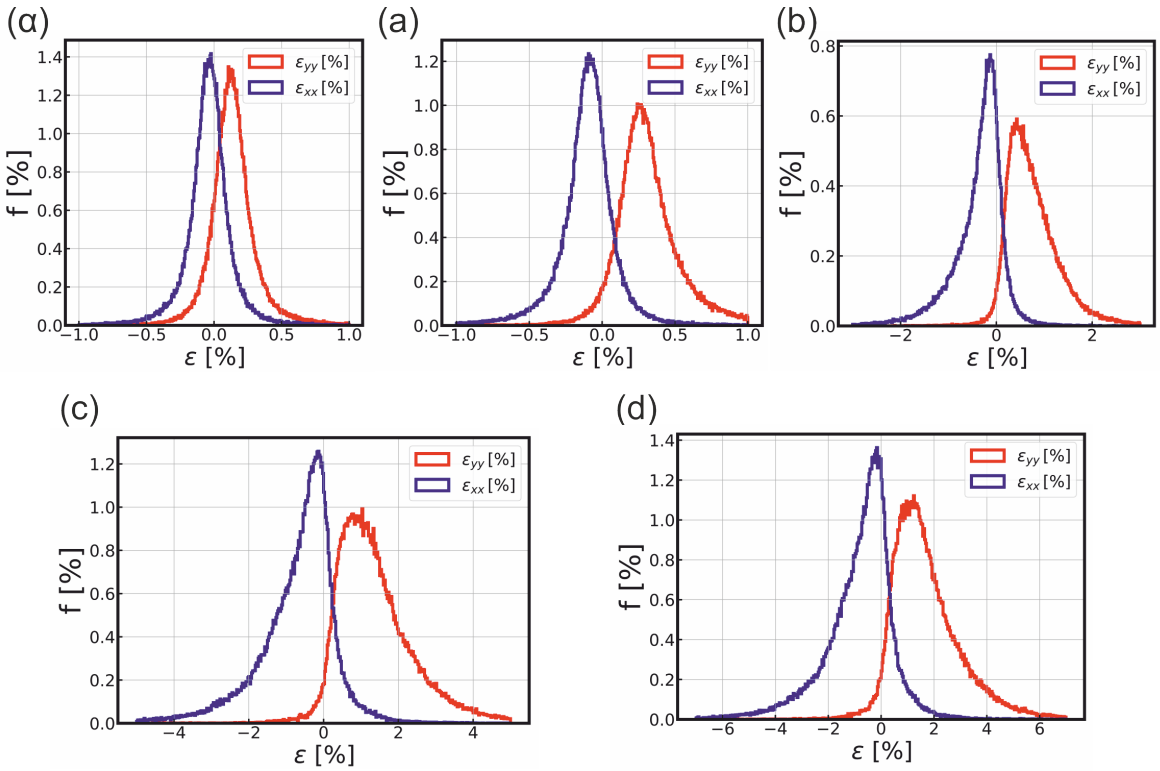

Figure 3.14. ε_{yy} and ε_{xx} histograms of the selected area of TDO specimen.

Although the limitation on the area development of non-45° bands, flat bands still lose visual intense with increasing strain. However; since colorbar scale expands at each load point, this intensity loss should be attributed to greater strain content on non-45° bands. The further straining over non-45° localization structures can also be spotted from emerging and expanding DIC invalidations (at point c and d) on the core of non-45° bands.

The evolution of negative axial strain field does not show a sharp change in terms of localization pattern through load point *b*,*c* and *d*. As observed at point a the severe localization starts with non-45° bands, and these bands grow in agreement with the microstructure as captured on ε_{yy} fields. No further localization structure apart from non-45° bands emerges at these points. This single banded pattern on ε_{xx} field indicates that Poisson contraction of RD tensioned MgAZ31 is majorly accomodated by non-45° bands.

Additionally in Figure 3.14, histograms that contain ε_{yy} and ε_{xx} distribution of the selected box of each load stage is presented as a quantitative approach. The first remarkable aspect regarding the histograms is the consistency with the histograms of the entire micro-DIC field shown in Figure 3.8. The trend and span of histogram of each load point (with an exception of point *a*) exhibits a stong similarity with the axial strain distribution of the overall TDO field. The strain heterogeneity accompanying with the emergence of early non-45° bands at point *a* in the selected region Figure 3.13(a) causes deviation from the overall histogram trend. Apart from this small variation, Figure 3.14 clearly signifies that the selected region is a representative area of the entire field. Thus, the statistical significance of the results found for the interested box is innately strengthened to portray overall behavior of the field with inherent microstructure.

3.5. EBSD results

A typical as received TDO specimen is prepared for Electron back scatter diffraction (EBSD) analysis. 625x415 μm^2 area from the gage section is scanned with 0.5 μm resolution. The aim is to reveal potential slip mechanisms operative on the TD face over different grains and grain clusters. Figure 3.15(a) and (b) present Schmid factor map of basal and prismatic slip mechanisms, respectively, on the TD surface with loading direction RD. Blue and red arrows on each picture indicate slip plane and slip direction respectievly. Note that ND-RD configuration of Schmid maps is 90° rotated version of the typical portrayal (e.g Figure 3.6).

The overall fashion on basal Schmid map 3.15(a) of TD-normal EBSD field is greater Schmid factor (∼0.3-0.5) on majority of relatively small grains clustered in the form of non-45° bands as observed on underlaying microstructure in Figure 3.13. To create a more clear visualization, small grain aggragates are confined with dashed lines. The considerable basal slip potential on non-45° structures clarifies the strain localization over these structures (Figure 3.13) in plastic regime. In a similar manner, the intense in-plane shear activity of non-45° bands (strong ν and ω_{xy} content) discussed in section 3.2.1 and 3.3.2 can be explained by grains with high Schmid factor.

For Schmid factor of prismatic slip, the resultant picture is consistent with the overall texture. Prismatic faces of a hexogonal crystal have considerable amount of resolved shear stress as a consequence of geometry of crystal structure. Comparing basal and prismatic Schmid maps, it can be concluded that prismatic slip system is prone to be activated in relatively large grains since basal Schmid is considerably small (~ 0.05) there.

3.6. Further Discussion

When the load on the sample is applied in the opposite sense to precipitate a completely different regime of strain accommodation with profuse tensile twinning (Aydiner and Telemez, 2014), though strain localization has been extremely sharp, interpretation has been straightforward with regard to (i) identification of the underlying micro-mechanism of meso- and macro-scale localization, and (ii) reconciliation of the surface data from the orthogonal faces of the sample to reach a volumetric understanding. Regarding the first, it was obvious that sharp ±45° bands were precipitated by twinning avalanches since out of the infinitely many ±45° planes, strain localization adhered to a singular pair. This pair matched the orientations of the operative tensile twin systems in the nominal orientation, sketched in Figure 3.16(a) Regarding the second, the localization structures ran across the bulk and orthogonal faces showed localization distributions that are compatible with a single volumetric deformation. This also implied that deformation on the surface is representative of the deformation

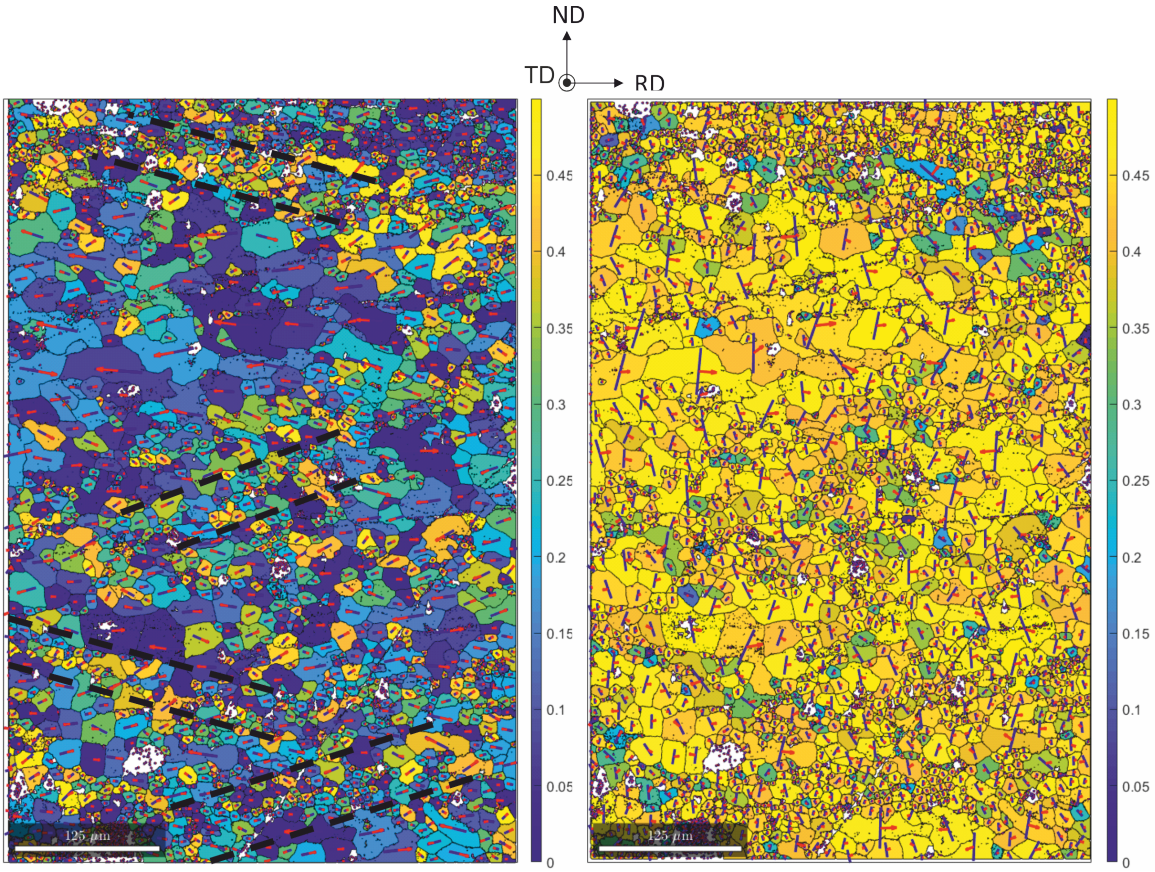

Figure 3.15. Schmid factor map of basal slip on TD surface

in parallel cross-sections in the bulk. The deformation in the RD-tension load path is more complex on both accounts; we will start with the issues and gradually sharpen our conclusions. The 3D aid (Figure 3.16) intended for description of both aspects is naturally in material coordinates ND-RD-TD, dubbed x'-y'-z'. If the Figure 3.16 box is taken as gage volume, for all intents and purposes, the reader can now overlay the TDO and NDO strain map pairs of Figure 3.6 on the respective orthogonal faces. Recall from Section 3.1 that this is a statistical (as opposed to an exact spatial) pairing; however, all arguments that follow will be over statistically-significant observations that relate to mechanisms.

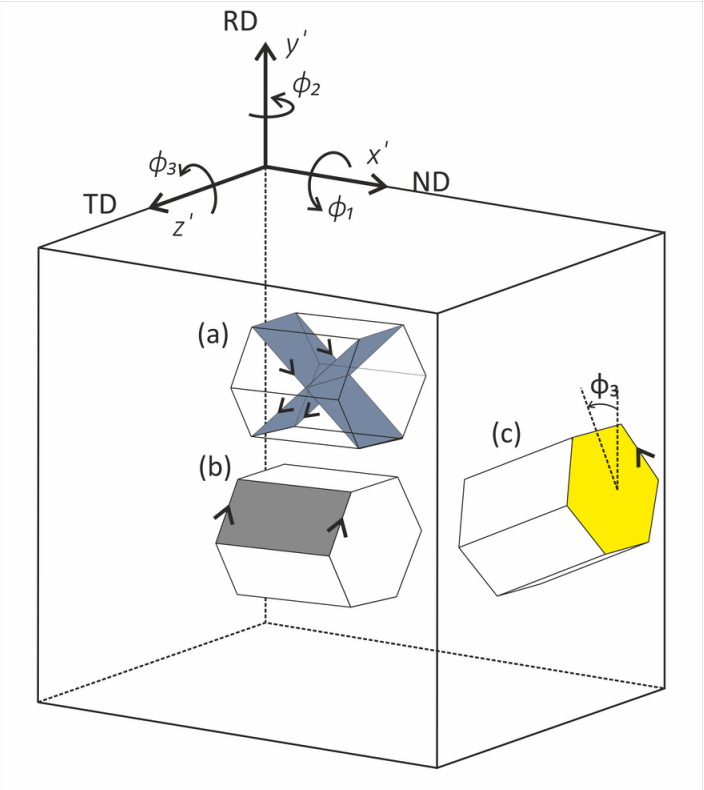

Figure 3.16. Unit cell representation of twin on parent $\{10\bar{1}2\}$ planes (a), prismatic slip on $\{10\bar{1}0\}$ plane (b), basal slip on $\{0001\}$ plane (c) in a generic rolled sample

3.6.1. Surface versus bulk deformation

Consider a representative volume in a deforming solid, large enough that the planar distributions on its cross-sections are also representative. If strain distributions are measured on orthogonal cross-sections of this volume, the statistics of the distribution in their common direction should agree . Reducing to the current case, TDO and NDO ε_{yy} histograms are supposed to agree if they are representative of the same volumetric deformation. Since lack of statistics is not a concern in these full-gage-section scans, the unmistakable shape and span disparity among ε_{yy} histograms of TDO and NDO surfaces indicate significant surface effects: Though the traction-free surface boundary condition does not conflict with the nominal uniaxial stress state, local states can be very different. Therefore, the lack of constraint in the out-of-plane direction leads to surface strain accommodation deviating from that in the bulk. Particularly at the

initial stages, lack of volumetric compatibility of TDO and NDO measurements are apparent through the investigation of localization structures as well. Consider the proposition over Figure 3.6 that flat localization traces on TDO and low-angle localization traces on NDO belong to the same "slab" of volumetric deformation. This will first be conflicted by the inconsistency ε_{yy} intensities (Section 3.3) and, secondly, by a more acute test yielded by volume preservation in these simple-shear (plasticity) structures: Local Poisson's ratios measured over the traces in the two orthogonal faces should add up to $\sim$1 (Equation 3.7) . Clearly, the very low $\bar{\nu}$ $\sim$0.1 realized in TDO-flat and NDO low-angle traces are decidedly not summing up to this value. From a general perspective, the fact that these are two different surface-mediated structures is consistent with their "out-of-plane shear" nature, since, in general, the zero-traction out-of-plane boundary condition ensures consistently high shear stress on such planes.

$$tr(\varepsilon) = 0 \Rightarrow \varepsilon_{x'x'} + \varepsilon_{y'y'} + \varepsilon_{z'z'} = 0 \Rightarrow \nu_{y'x'} + \nu_{y'z'} = 1 \Rightarrow \nu_{yx}^{TDO} + \nu_{yx}^{NDO} = 1 \quad (3.7)$$

The non-45° bands of the TDO face, on the other hand, show signs of being volumetrically compatible when they are paired with the second wave of bands on the NDO surface that caused segregation and appear with some angular disorder. Firstly, the timing fits: They both appear (Figure 3.6) at several localities at load point a; then spread and intensify over the rest of the loads. Second, trends in Poisson's ratios are coherent. $\bar{\nu}$ filtered over TDO is around 0.7-0.8 (Figure 3.11). Over NDO, $\bar{\nu}$ of high strain structures are climbing toward 0.2 (point d, Table 3.2) as the second wave becomes predominant, from a significantly lower value ($\sim$0.07) (Table 3.5) that corresponded to the initial low-angle surface structures. Further, the macroscopic segregation over NDO face can be visualized over the TDO maps if a vertical cut is considered, exemplified over Figure 3.7. Over this cut, low-strain segments are evident, as the one marked in the middle of the span, lying between the high-strain traces of non-45° bands. Thus, non-45° bands on TDO and segregated bands on NDO are judged to be traces of the same family of structures. The mechanistic agreement does not, however, imply the surface effect is null in their operation. In fact, based on Figure 3.8 histograms, the activity level of these structures are augmented on the NDO surface on which they

shear out-of-plane. It is reasonable that their operation is favored further by the lack of out-of-plane constraint on this surface. The intense surface roughening reflected in widespread DIC invalidations (Figure 3.7, NDO column), far superseding that on the TDO surface, conforms to this assessment.

3.6.2. On the microstructure of non-45° bands

These microstructures themselves are usually called shear bands, since they are formed by localized shear during the forming process [34, 42]. Once formed, they are not typically eliminated by further annealing [32]. The microstructural small grain bands over which the non-45° shear bands formed are observed in Magnesium and its light alloys (AZ31, rare-earth). There is consensus that these bands form due to recrystallization at heavy deformation sites during rolling though the exact mechanism seems to be a source of debate rotational dynamic recrystallization [43, 44], recrystallization at double-twinning sites [33]. Regardless, what is directly relevant is that (i) they are typical of hot-rolled plates of Magnesium and its many alloys ([32] terms the mesoscale patterns on the TDO surface "rhombic microstructure" for AZ31; one can spot these on bare surface images without the strain maps as well, e.g., careful consideration of Figure 2.6(d)) and (ii) strain localization on them is attributed to micro-texture. More precisely, while the preferred orientations would have small Schmid factors (SF) for basal slip (zero for Figure 3.16(b) nominal orientation), these small grains are off-texture and have high SFs for basal slip. (Every polycrystal has off-texture grains, which don't show in pole figures due to their low volume fraction, and also typically eliminated in the orientation distribution function fit as outliers. Note in this case, though, the outliers are spatially connected.) Since basal slip is multiple factors easier than the other mechanisms, shear is localized into these bands. In addition to the adequate EBSD measurements in literature [**?**, 30], our representative-area measurement (3.15, plot in terms of basal-slip SF) also shows the existence of many grains with operable SFs (0.1) for the easy basal slip. Figure 3.15 shows that particularly-high-SF grains are typically smaller and coarsely clustered in bands (dashed lines are added as visual aids). These are surrounded by larger grains that tend to obey the nominal-

orientation with low basal-slip SF. The coarse nature of the micro-texture bands likely conform to the variability observed in the non-45° shear structures in terms of breadth and orientation both on TDO and NDO surfaces.

3.6.3. On micro-mechanisms that underlie localization structures

Rolled Magnesium has one of the sharpest overall textures, akin to a single crystal with its preferred c-axis alignment. Thus, attempting to interpret the predominant (slip/twinning) micromechanism that underlies a particular transgranular localization over the nominal orientations (Figure 3.16) is a useful exercise in a statistical sense. This worked perfectly for the behavior in the opposite load path [3], where one mechanism (tensile-twin) dominated the strain accommodation with unmistakable cues in addition to frequent observation of the twins themselves in the images. In the RD-tension load path considered here, however, we have just remarked that micro-texture emerges as a dominant factor in the most striking strain localization structures (Section 3.6.2) and the behavior is clearly more compound. Fortunately for a more detailed understanding, while this study bridges meso- and macro-scales, there has been a recent scanning DIC implementation that bridged micro- and meso-scales with true intragranular resolution by Orozco-Caballero [15] in which the observation surface coincided with the NDO sample. Their study is, first, striking in revealing how compound the deformation behavior is by identifying the individual activity of multiple slip systems (basal, prismatic, type-II pyramidal) and the tensile twin, which still shows occasional operation in this load path. Second, in the one transgranular band in their window, they identify the predominant mechanism as basal slip. It is further noted that, among the grains in which basal slip is not geometrically favored, (non-basal) slip activity is augmented if the grain lies in the path of basal activity. The consequence is that the transgranular band is micro-mechanistically compound but basal slip is the primary mediator. The shape and orientation of this band is reminiscent of our second-wave bands on NDO: in a broad sense, it is oriented normal to the load but has a slightly wavy pattern (more obvious in their large binning window (2.8 μm) plot, akin to the measurement scale here) that negotiates through some geometrically easier

grains/interfaces.

For completeness, let us try to provide an explanation to the surface-specific localization structures that we explained at point a, as well. For these, interpretation over the broad texture (nominal orientations) appears to be adequate given their homogenous and ordered distributions over the entire structure. Over the Figure 3.16(c) unit cell, it is shown that even limited misorientations from the nominal orientation will yield operable Schmid Factors (SF 0.15 for ϕ_3=10°) for basal slip. Despite the slanted activation, it is easy to show that for these $\nu_{y'z'}$=0, complying with the very low local Poisson's ratio (∼0.07) observation on the NDO surface.Figure 3.16(b) shows a prismatic slip over the nominal orientation. The very high Schmid factors are in favor (0.433 for this particular unit cell; 0.5 available for the ∼ equally likely orientation that is rotated by 15° ϕ_1 about though prism the harder mechanism whose bulk activation follows basal (see [45], IPT sample). If there is strain localization mediated by prism slip in likeness to Figure 3.16(c), it would appear flat on TDO face and clearly satisfy low Poisson's ratio.

Our operating theory on the surface-mediated structure than goes as follows: First, as a general argument, deformation starts at the free surface that ensures a zero principal stress and consequently high shear directions that are out-of-plane. Second, at this stage, each surface uses whatever out-of-plane mechanism is available to it. So, though Schmid factors of the proposed mechanisms (Figure 3.16(b) or (c)) do not depend on a choice of surface (or being in the bulk for that matter), the one that works out-of-plane seem to be favored and favored to localize on a respective surface. Accordingly, we postulate that basal and prism slip underlie NDO and TDO surface-mediated structures, respectively. The fact that TDO traces carry much less strain is compatible with the harder activation of prism slip and its more homogenous operation [15]. We emphasize that the basal/prism naming only pertains to the major element; any transgranular strain localization is bound to be compound.

4. CONCLUSION

MgAZ31 with rolling-texture shows strong tension-compression anisotropy. $\{10\bar{1}2\}$ tensile twin is the dominant mechanism that determines the overall character of deformation ($\pm$ 45° bands) under RD-compression or ND-tension. In the opposite sense of loading i.e. ND-compression or RD-tension, elements governing the deformation character in the absence of profuse twinning become complicated. To identify deformation characteristics under this type of load configuration, two dogbone samples respectively cut from TD-normal (TDO) and ND-normal (NDO) faces of a rolled plate are subjected to uniaxial tensile testing along RD up to 1.5 % of average axial strain. Strain localization patterns are investigated by in-situ multiscale DIC method in early plastic regime. The two samples taken intentionally from two orthogonal faces of the rolled material allow assessing the nature of deformation in 3D. Further, macro-DIC measurements are utilized at the side surfaces to verify statistical equivalance of both specimens. Micro-DIC measurements feature area scanning and yield combination strain maps that provide both high resolution and high statistics.

Over the TDO samples, flat strain localization patterns are observed of the combination strain maps at the very early points of plasticity. Then, strain accommodation is dominated by localization structures in the form of non-45° bands at later stages of deformation. For $ND^{\perp}$ surface, localization patterns start with a similar flat band pattern -with greater intensity- later horizontal thick bands with great axial strain intensity emerge. Strain accommodation by these localization patterns on both observation planes ($TD^{\perp}$ and $ND^{\perp}$) can be summarized as follows: Non-45° bands are major localization character of $TD^{\perp}$. The emergence of these structures generates considerable heterogeneity at first time, but at further stages of plasticity non-45° bands show homogenizing tendency. On the other hand, thick horizontal structures of strain localizations create significant strain heterogeneity in the overall field. This sharp heterogeneity of localization even shows itself at macroscale.

For the quantitative aspects of strain localization patterns at both faces, ε_{yy} and ω_{xy} are employed as limiting parameters in data filtering. Flat bands of early deformation stages on both surfaces have considerably small Poisson's ratio ($\nu \sim 0.1$) indicating that collobrative activity of this structures can be identified as out-of-plane shear.Conversely, non-45° bands with intense ω_{xy} content exhibit $\nu \sim$ 0.7-0.8. This significant ν content points that non-45° bands show in-plane shear activity. In fact, thick horizontal bands have $\nu \sim 0.2$ which implies that (ν_{ND}+ν_{TD}∼1) out-of-plane thick strain localizations are projection of non-45° bands on $ND^{\perp}$ face.

However, non-45° bands and thick horizontal localizations are not volumetrically compatible for early flat localization pattern on both $TD^{\perp}$ and $ND^{\perp}$ planes. They both have Poisson's ratio near zero which does not agree with volume preservation of bulk deformation. The character of these flat bands can be explained as surface effect. More precisely, at very initial stages of plastic deformation constraint-free condition on surfaces basically facilitates out-of plane shear activity over these structures.

As for individual slip mechanisms of localization structures, EBSD results on $TD^{\perp}$ surface show that the off-basal microtexture on relatively small grains clustered in the from of non-45° structures governs heavy basal slip activity on non-45° bands. For flat localization patterns, considering the governing texture, prismatic slip activity is primary component of $TD^{\perp}$ face flat bands while, for the $ND^{\perp}$ face flat bands, basal slip over grains that deviate slightly from the nominal texture is the leading mechanism.

5. FUTURE WORK

As observed at both TDO and NDO samples at early points of deformation there are strain localizations in the form of flat bands giving Poisson's ratio of 0.1 (In this study, flat structures are concluded as a consequence of surface effect). In fact, this typical emergence of flat localization structures is also observed at several materials like Titanium, Nickel and NiTi shape memory alloy. For future studies the occurrence of these localization structures can be investigated. For now, the most viable method to reveal the nature of these localizations can be an in-situ early stage deformation experiment. Namely, a sample specimen is either tensioned or compressed up to average strain of 0.3-0.4 % followed by an unload. Then with an EBSD study over a large region of the specimen KAM map of the field could be provided. Employing the KAM map of the deformed sample, regions where dislocation density is relatively greater could show up. Thus, crystallographic orientations of the grains under high dislocation regions can be revealed and active slip mechanisms could be determined.

Furthermore, an as-received NDO specimen could be prepared for EBSD analysis to disclose potential slip mechanisms on ND face. However; since ND face does not have any characteristic morphology as TD face has, further uniaxial tension experiment is required to comprehend active slip mechanisms under localization structures. This approach may present collobrative deformation mechanisms producing mesoscale strain heterogeneities in volumetric sense.

In addition to further post-mortem analysis on repeated TDO/NDO tensioned experiments, in order to present 3D deformation nature of AZ31 under c-axis compression type of loading, TD tensioned RDO samples can be potentially studied. This type of sample-load configuration will show the localization behavior of the material at both elastic to plastic transition region and early plastic region. Doing so, volumetric representation of deformation trend can be obtained.

REFERENCES

1. Avedesian, M. M. and H. Baker, *ASM Specialty Handbook: Magnesium and Magnesium Alloys*, ASM International, USA, 1999.

2. Christian, J. and S. Mahajan, "Deformation twinning", *Progress in Materials Science*, Vol. 39, No. 1-2, pp. 1–157, 1995.

3. Aydiner, C. C. and M. A. Telemez, "Multiscale deformation heterogeneity in twinning magnesium investigated with in situ image correlation", *International Journal of Plasticity*, Vol. 56, pp. 203–218, 2014.

4. Gloaguen, D., G. Oum, V. Legrand, J. Fajoui, M.-J. Moya, T. Pirling and W. Kockelmann, "Intergranular Strain Evolution in Titanium During Tensile Loading: Neutron Diffraction and Polycrystalline Model", *Metallurgical and Materials Transactions A*, Vol. 46, No. 11, pp. 5038–5046, November 2015.

5. Barkia, B., V. Doquet, J. P. Couzinié, I. Guillot and E. Héripré, "In situ monitoring of the deformation mechanisms in titanium with different oxygen contents", *Materials Science and Engineering: A*, Vol. 636, pp. 91–102, 2015.

6. Hosford, W. F., *Mechanical Behavior of Materials*, Cambridge University Press, 32 Avenue of the Americas, New York, NY 10013-2473, USA, 2010.

7. Proust, G., C. N. Tomé, A. Jain and S. R. Agnew, "Modeling the effect of twinning and detwinning during strain-path changes of magnesium alloy AZ31", *International Journal of Plasticity*, Vol. 25, No. 5, pp. 861–880, May 2009.

8. Kocks, U. F., C. N. Tomé and H. R. R. Wenk, *Texture and Anisotropy: Preferred Orientations in Polycrystals and Their Effect on Materials Properties*, Cambridge University Press, 2000.

9. Agnew, S. R. and Ö. Duygulu, "Plastic anisotropy and the role of non-basal slip in magnesium alloy AZ31B", *International Journal of Plasticity*, Vol. 21, No. 6, pp. 1161–1193, June 2005.

10. "Hardening evolution of AZ31B Mg sheet", *International Journal of Plasticity*, Vol. 23, No. 1, pp. 44–86, 2007.

11. Kleiner, S. and P. J. Uggowitzer, "Mechanical anisotropy of extruded Mg–6% Al–1% Zn alloy", *Materials Science and Engineering: A*, Vol. 379, No. 1-2, pp. 258–263, 2004.

12. Efstathiou, C., H. Sehitoglu and J. Lambros, "Multiscale strain measurements of plastically deforming polycrystalline titanium: Role of deformation heterogeneities", *International Journal of Plasticity*, Vol. 26, No. 1, pp. 93–106, 2010.

13. Hazeli, K., J. Cuadra, P. A. Vanniamparambil and A. Kontsos, "In situ identification of twin-related bands near yielding in a magnesium alloy", *Scripta Materialia*, Vol. 68, No. 1, pp. 83–86, 2013.

14. Kapan, E., N. Shafaghi, S. Ucar and C. C. Aydiner, "Texture-dependent character of strain heterogeneity in Magnesium AZ31 under reversed loading", *Materials Science and Engineering: A*, Vol. 684, pp. 706–711, 2017.

15. Orozco-Caballero, A., D. Lunt, J. D. Robson and J. Quinta da Fonseca, "How magnesium accommodates local deformation incompatibility: a high-resolution digital image correlation study", *Acta Materialia*, Vol. 133, pp. 367–379, 2017.

16. Barnett, M. R., M. D. Nave and A. Ghaderi, "Yield point elongation due to twinning in a magnesium alloy", *Acta Materialia*, Vol. 60, No. 4, pp. 1433–1443, 2012.

17. Beyerlein, I., L. Capolungo, P. Marshall, R. McCabe and C. Tomé, "Statistical analyses of deformation twinning in magnesium", *Philosophical Magazine*, Vol. 90, No. 16, pp. 2161–2190, 2010.

18. Héripré, E., M. Dexet, J. Crépin, L. Gélébart, A. Roos, M. Bornert and D. Caldemaison, "Coupling between experimental measurements and polycrystal finite element calculations for micromechanical study of metallic materials", *International Journal of Plasticity*, Vol. 23, No. 9, pp. 1512–1539, 2007.

19. Padilla, H. A., J. Lambros, A. J. Beaudoin and I. M. Robertson, "Relating inhomogeneous deformation to local texture in zirconium through grain-scale digital image correlation strain mapping experiments", *International Journal of Solids and Structures*, Vol. 49, No. 1, pp. 18–31, 2012.

20. Reed-Hill, R. E., "Institute of Metals Division - A study of the {1011} and {1013} Twinning Modes in Magnesium", *Organization: The American Institute of Mining, Metallurgical, and Petroleum Engineers*, p. 5, 1961.

21. Yoshinaga, H., T. Obara and S. Morozumi, "Twinning deformation in magnesium compressed along the C-axis", *Materials Science and Engineering*, Vol. 12, No. 5, pp. 255–264, 1973.

22. Wonsiewicz, B. C. and B. W. A, "Plasticity of Magnesium Crystals", *Trans. Metall. Soc. Metals*, 1967.

23. Barnett, M. R., Z. Keshavarz, A. G. Beer and X. Ma, "Non-Schmid behaviour during secondary twinning in a polycrystalline magnesium alloy", *Acta Materialia*, Vol. 56, No. 1, pp. 5–15, 2008.

24. Crocker, A. G., "Double twinning", *Philosophical Magazine*, Vol. 7, No. 83, pp. 1901–1924, 1962.

25. Couling, S. L., J. F. Pashak and L. Sturkey, "Unique deformation and aging characteristics of certain magnesium-base alloys", *Trans. Amer. Soc. Metals*, Vol. 51, 1959.

26. Barnett, M. R., "The challenge of inhomogeneous deformation in Mg and its al-

loys", *Material Science Forum*, Vol. 618-619, pp. 227–232, 2009.

27. Kim, H., J.-H. Lee, C. Lee, W. Bang, S. Ahn and Y. Chang, "Shear band formation during hot compression of AZ31 Mg alloy sheets", *Materials Science and Engineering: A*, Vol. 558, pp. 431–438, December 2012.

28. Sun, D. K. and C. P. Chang, "Microstructural study of strain localization in a compressed Mg-3Al-1Zn alloy", *Materials Science and Engineering A*, Vol. 603, pp. 30–36, 2014.

29. Barnett, M. R., M. D. Nave and C. J. Bettles, "Deformation microstructures and textures of some cold rolled Mg alloys", *Materials Science and Engineering A*, Vol. 386, No. 1-2, pp. 205–211, 2004.

30. Sandlöbes, S., S. Zaefferer, I. Schestakow, S. Yi and R. Gonzalez-Martinez, "On the role of non-basal deformation mechanisms for the ductility of Mg and Mg-Y alloys", *Acta Materialia*, Vol. 59, No. 2, pp. 429–439, 2011.

31. Chun, Y. B. and C. H. J. Davies, "Texture effects on development of shear bands in rolled AZ31 alloy", *Materials Science and Engineering A*, Vol. 556, pp. 253–259, 2012.

32. Bach, F. W., M. Rodman, A. Rossberg, B. A. Behrens and G. Kurzare, "Macroscopic damage by the formation of shear bands during the rolling and deep drawing of magnesium sheets", *JOM*, Vol. 57, No. 5, pp. 57–61, May 2005.

33. Yi, S., I. Schestakow and S. Zaefferer, "Twinning-related microstructural evolution during hot rolling and subsequent annealing of pure magnesium", *Materials Science and Engineering A*, Vol. 516, No. 1-2, pp. 58–64, 2009.

34. Victoria-Hernandez, J., S. Yi, J. Bohlen, G. Kurz and D. Letzig, "The influence of the recrystallization mechanisms and grain growth on the texture of a hot rolled AZ31 sheet during subsequent isochronal annealing", *Journal of Alloys and Com-*

pounds, Vol. 616, pp. 189–197, 2014.

35. "The role of deformation twinning in the fracture behavior and mechanism of basal textured magnesium alloys", *Materials Science and Engineering A*, Vol. 600, pp. 145–152, 2014.

36. Lentz, M., M. Risse, N. Schaefer, W. Reimers and I. J. Beyerlein, "Strength and ductility with $\{10\bar{1}1\}$-$\{10\bar{1}2\}$ double twinning in a magnesium alloy", *Nature Communications*, Vol. 7, p. 11068, April 2016.

37. Hunter, J. D., "Matplotlib: A 2D graphics environment", *Computing in Science and Engineering*, Vol. 9, No. 3, pp. 99–104, 2007.

38. Jones, E., T. Oliphant and P. Peterson, "SciPy: Open Source Scientific Tools for Python", *Computing in Science and Engineering*, Vol. 7, 2001.

39. Sutton, M. A., J. J. Orteu and H. W. Schreier, *Image correlation in mage Correlation for Shape, Motion and Deformation Measurements: Basic Concepts,Theory and Applications*, Springer, New York, NY, 2010.

40. Vendroux, G. and W. G. Knauss, "Submicron deformation field measurements: Part 1. Developing a digital scanning tunneling microscope", *Experimental Mechanics*, Vol. 38, No. 1, pp. 18–23, 1998.

41. Kang, J., D. S. Wilkinson, R. K. Mishra, W. Yuan and R. S. Mishra, "Effect of inhomogeneous deformation on anisotropy of AZ31 magnesium sheet", *Materials Science and Engineering: A*, Vol. 567, pp. 101–109, 2013.

42. Zhang, Z., M. P. Wang, N. Jiang and S. Zhu, "Formation of shearing bands in the hot-rolling process of AZ31 alloy", *Journal of Alloys and Compounds*, Vol. 512, No. 1, pp. 73–78, 2012.

43. Ion, S. E., F. J. Humphreys and S. H. White, "Dynamic recrystallisation and

the development of microstructure during the high temperature deformation of magnesium", *Acta Metallurgica*, Vol. 30, No. 10, pp. 1909–1919, 1982.

44. Wang, Y., Y. Xin, H. Yu, L. Lv and Q. Liu, "Formation and microstructure of shear bands during hot rolling of a Mg-6Zn-0.5Zr alloy plate with a basal texture", *Journal of Alloys and Compounds*, Vol. 644, pp. 147–154, 2015.

45. Agnew, S. R., C. N. Tomé, D. W. Brown, T. M. Holden, S. C. Vogel, C. N. Tome, D. W. Brown, T. M. Holden and S. C. Vogel, "Study of slip mechanisms in a magnesium alloy by neutron diffraction and modeling", *Scripta Materialia*, Vol. 48, No. 8, pp. 1003–1008, 2003.

APPENDIX A: COMBINATION MAPS OF ALL DEFORMATION STAGES

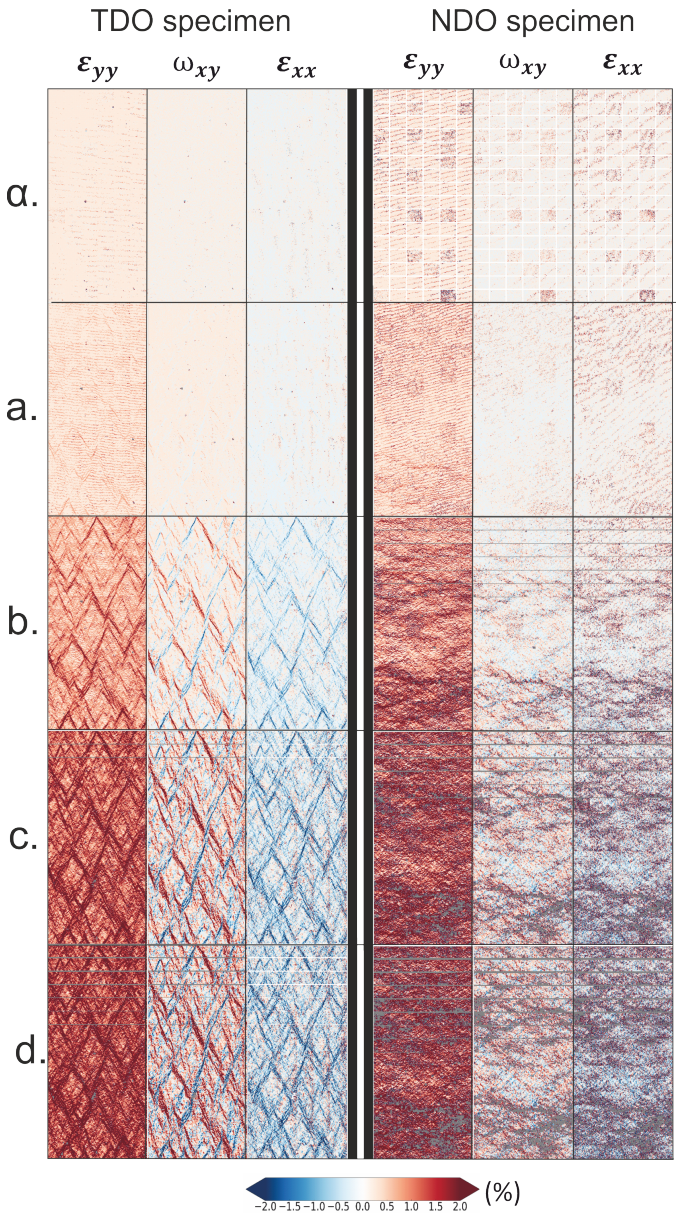

Figure A.1. Full size micro-DIC combination maps of load point α-d for axial strain (ε_{yy}), rotation (ω_{xy}) and transverse strain (ε_{xx}) for both TDO and NDO samples at equivalent stages